# Manipulation of magnetic nanoparticles with rotating and pulsed magnetic field

by

Laszlo Bodnar

B.S., University of Szeged, 2014
M.S., University of Szeged, 2017

A THESIS

submitted in partial fulfillment of the requirements for the degree

MASTER OF SCIENCE

Department of Chemistry
College of Arts and Sciences

KANSAS STATE UNIVERSITY
Manhattan, Kansas

2019

Approved by:

Major Professor
Viktor Chikan

# Copyright

# Abstract

In the bioengineering field, magnetic nanoparticles are investigated for a variety of reasons. Magnetic nanoparticles in combination with magnetic fields are used as drug carriers, MRI contrast agents and therapeutic agents for cancer treatment. This research requires the cooperation of several research groups from different fields and therefore, a portable magnetic field generating device is often required.

In the first part of this thesis the construction of a pulsed magnetic field generating device is described. The instrument is portable, easy to use and the commercial production of it is feasible. The device is based on two Bitter-type electromagnets driven by a resonant circuit. The bore of the coils can accept a test tube or adherent cell culture tube. The planned experiments involve drug release experiments performed on 5(6)-Carboxyfluorescein containing liposomes and cell viability assays using adherent cell cultures treated with an antibiotic drug and magnetic nanoparticles. To generate the magnetic pulse, a capacitor is discharged via a spark-gap switch, triggered by a high-voltage trigger spark generator. The device is controlled by a programmable logic controller (PLC) and an Arduino unit. The profile of the magnetic field generated by the coils was obtained by placing a high resolution magnetic viewing film into the coils.

In the second part of this thesis, the creation and testing of a rotating field hyperthermia device is described. A perpendicular coil pair was constructed and driven through a resonant circuit. Iron-oxide nanoparticles were used to investigate the heating efficiency of the system. Magnetic heating was observed, however, the resistive heating of the coil material and the radiative heat transfer from the coil to the sample make the temperature measurement results unreliable. A more sophisticated experimental setup is needed in which the cooling of the coils and the thermal

insulation of the sample is possible. Based on our results we presume that, with the aforementioned issues addressed, rotating magnetic fields can be a better alternative to the widely used alternating magnetic fields.

# Table of Contents

# List of Figures

# List of Abbreviations

| | |
|---|---|
| MRI: | Magnetic resonance imaging |
| AMF: | Alternating magnetic field |
| RMF: | Rotating magnetic field |
| NHMFL: | National High Magnetic Field Laboratory |
| PLC: | Programmable logic controller |
| DC: | Direct current |
| AC/DC converter: | Alternating current to direct current converter |
| IR: | Infrared |
| SAR: | Specific absorption rate |
| PLA: | Polylactic acid |
| KSU: | Kansas State University |
| ITS: | Information Technology Services |
| NMR: | Nuclear Magnetic Resonance |

# Acknowledgements

I would like to thank my major professor, Professor Viktor Chikan. He gave me the opportunity to come to the United States, work in his research group and broaden my horizon. He was and is an endless source of motivation and a person to whom I could always turn with my questions.

I would like to thank all the members in my committee, Professor Christine Aikens, Professor Stefan Bossmann and Professor Michael J. O'Shea. Without their invaluable insight and advice on my work I would not have been able to get this far.

I would like to thank Dr. Jack Toth at the National High Magnetic Field Laboratory for providing us with the material we could use to construct our electromagnets.

I would like to thank Professor Paul Smith for helping me navigate through the maze of departmental requirements and making sure that I fulfilled most of them.

I would like to express my gratitude to Professor Santosh Aryal for his generous help, allowing us to use their fiber optic temperature sensor and IR camera.

I would like to thank Ron Jackson and Tobe Eggers, for without their expertise, none of my work would have been realized.

I would like to also thank Matthew Davis, who as an undergraduate researcher provided useful help and insight during my research.

Last, but not least, I would like to thank my fiancée, Eva Dobó. Without her inexhaustible patience, support and love I would have not been able to overcome the challenges of the past three years.

# Chapter 1 - Introduction

With advances made in nanotechnology, medical application of nanomaterials is a highly sought after area.[1] In the bioengineering field, magnetic nanoparticles are investigated for a variety of reasons. These reasons include the use of mechanical and thermal effects from these particles for therapeutic use (mechanical force[2], magnetic hyperthermia[3,4,5], ultrasound generated with such particles[6,7,8] andexternally triggered drug delivery[9,10,11]). Magnetic nanoparticles are used as drug carriers, MRI contrast agents and therapeutic agents for cancer treatment.[12,13] Studies have shown that surface modified nanoparticles are not only able to deliver a payload to a target, but are capable of enhancing the cells' uptake of the drugs. Such particles can increase cell membrane permeability and this effect can be externally triggered in several ways.[14,15] When exposed to an electric field, the transmembrane potential of the cells changes and nanometer sized holes are created. When the nanoparticles are actuated by an electric field, the method is called electroporation or iontophoresis. The invasive nature is one of the drawbacks of this technique, as electrodes must be inserted into the target tissue to induce the electric field. It might also cause irreversible permeability increase, which leads to cell death. A safer solution is to use another field, which does not require implanted electrodes to induce an electric field locally. A magnetic field that changes with time can be used as such a field and the technique utilizing it is called magnetoporation.[16,17] A magnetic field has several advantages over an electric field. The magnetic field is noninvasive, its penetration depth is superior to that of the electric field's, it can be operated in oscillating or pulsed modes and the targeted area can be dynamically changed during treatment. The electric field induced by a changing magnetic field is described by the Maxwell-Faraday equation (1):

$$\nabla \times E = -\frac{\partial B}{\partial t} \quad (1)$$

where ∇ is the curl operator, *E* is the induced electric field (dependent on time and position), *B* is the magnetic field strength and *t* is the time. Based on this equation, we can say that in order to induce a strong electric field in the target tissue, the amplitude of the magnetic field must change rapidly. High current pulsed magnetic fields fulfill this requirement.

Another important application of alternating magnetic fields (AMF) is found in magnetic hyperthermia. When superparamagnetic nanoparticles are exposed to an external AMF, their dipole moment tries to align with the magnetic field vector. This orientation change can happen in two ways. When the particles' dipole moment cannot reorient itself without the rotation of the crystal, the external field will move the whole particle. This process is called Brownian relaxation. Another relaxation process is when the dipole moment can rotate in response to the magnetic field, without the particle having to move. This mechanism is called the Néel relaxation. Both mechanisms are present when superparamagnetic nanoparticles are exposed to AMF. As the particle size gets larger, Brownian relaxation becomes dominant, whereas with increasing AMF frequency the Néel relaxation becomes the primary relaxation process.[18,19] Triggered drug release can be achieved through hyperthermia several ways. The two most widely used methods are attaching drug molecules to the nanoparticle surface with thermosensitive linkers, or loading the nanoparticles into a thermosensitive carrier system like liposomes.[9] In the first case, the bond between the linker and the drug molecule breaks due to the elevated temperature, thus releasing the payload due to an external triggering effect. In the case of liposome drug delivery, the magnetic nanoparticles are either attached to the surface of the lipid bilayer, loaded into the liposome, or embedded into the bilayer. When the external magnetic field is applied, the local heating of the

magnetic nanoparticles will cause the liposomes to undergo a transformation between their gel and liquid phase, increasing membrane permeability and leading to drug release.[20,21]

The mechanical force of the nanoparticles can also be utilized to achieve triggered drug release.[2,8,11] The motion of the nanoparticles can destabilize the lipid membrane, leading to the on demand release of the payload. This effect occurs at lower frequencies (~ 20 000 Hz) than what is usually needed for magnetic hyperthermia (~100 000 Hz) and below the transition temperature of the lipid bilayer. With lower frequency and temperature, the risk of doing harm to healthy cells during the treatment is significantly lower. If the frequency of the motion of the nanoparticles is above 20 kHz and the particles can create mechanical waves in the medium, they will generate ultrasound. The cavitation effect of the ultrasound waves can also lead to the destabilization of the liposome membrane and can be used as a trigger mechanism.

The development of new treatment methods based on these effects require the cooperation of research groups from several fields. Physicists are needed to explain the underlying principles along which we can design our drug delivery systems. Chemists create the nanoparticles and carriers and prove the viability of the concept. Once the method is deemed usable, biologists, biochemists and medical professionals are needed to perform *in vitro* and *in vivo* experiments, in order to make the system safe and operable in biological media. A serious obstacle in the way of such cooperation had been the stationary nature of equipment in each research group. Biological samples cannot always be transferred to a different laboratory and the devices generating the magnetic field are immovable most of the time, due to their sheer size and the need of a cooling system.

Our goal was to create an instrument that is capable of generating a strong pulsed magnetic field that is portable and easy to use for even those who are not familiar with the principles of

magnetic field generation. We created a system that is able to generate an under dampened magnetic pulse in the frequency regime of 20000-30000 Hz, with two Bitter coils in series as part of a resonant circuit. One of the coils was made to possess Helmholtz-coil like characteristic, the other one resembles an anti-Helmholtz-coil. In a perfect Helmholtz-coil, the overlap of the individual magnetic fields of the two half coils result in a highly homogeneous magnetic field, while the result of the overlap in case of a perfect anti-Helmholtz coil creates a highly inhomogeneous field with large magnetic field gradient (Figure 1). Therefore, we expected the Helmholtz-like coil to generate a stronger, more homogeneous magnetic field and the anti-Helmholtz-like coil to generate a larger magnetic field gradient. The spatial profile of the magnetic field inside the Helmholtz-like coil is highly homogeneous, while the anti-Helmholtz-like coil generates a highly inhomogeneous magnetic field.

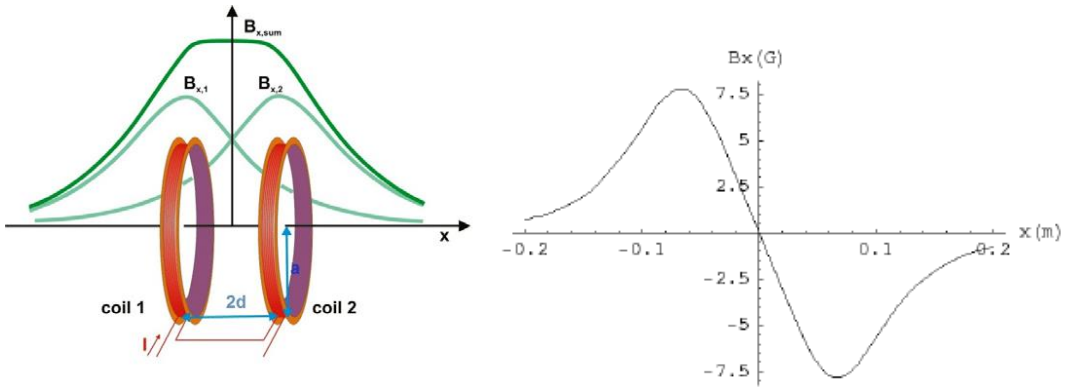


**Figure 1 The z component of the magnetic field along the x axis of the coil (Left: Helmholtz coil[22], Right: anti-Helmholtz coil[23])**

To induce drug release through magnetic hyperthermia, we explored the capabilities of rotating magnetic fields (RMF). The commonly used magnetic fields are effective, but there is a strong impetus to reduce treatment times by making the methodology more effective. The challenge is that as a result of the oscillating nature of the field, there are times when the field amplitude is zero therefore it is more desirable to manipulate the magnetic field direction and not

its amplitude. In this area, utilizing a rotating magnetic field could prove to be a better choice. Another problem with typical magnetic field generators is that the alternating magnetic fields is rather inhomogeneous leading to non-uniform heating. To address these challenges, a rotating magnetic field apparatus is proposed here with the integration of Helmholtz coil pairs. Solenoid coil pairs with soft-magnetic core have been used to produce homogeneous rotating magnetic field and to induce hyperthermia through the rotation of nanorods.[4] Unfortunately, the heating of the core and the non-linear nature of the magnetic field make these coils less viable for real life applications[24]. As an alternative, we aim to implement two Helmholtz coils in a perpendicular arrangement, to produce a homogeneous rotating magnetic field with a scalable apparatus[25] that can be used either in pulsed or continuous mode.

# Chapter 2 - Construction of the Bitter-coils

## 2.1 Design of the electromagnets

During the design of the electromagnet, several factors were taken into consideration. The design needed to be sturdy, simple and modular. The coil had to be able to conduct high frequency current without significant losses and heating. The goal was to perform drug internalization experiments on adherent cell line samples and drug release experiments on liposome samples. Both of these applications required the bore in the center of the coil to be large enough so that a test tube or an adherent cell culture tube could be placed inside it.

The minimization of ohmic losses at high frequency application made the use of round wire solenoids unfeasible. Due to the skin effect, high frequency current is localized and travels near the surface of the conductor, decreasing the effective cross section. The skin depth can be calculated with the following formula:

$$\delta = \sqrt{\frac{2 \cdot \rho}{2 \cdot \pi \cdot \nu \cdot \mu_0 \cdot \mu_r}} \tag{2}$$

where $\rho$ is the resistivity of the material in $\Omega \cdot m$, $\nu$ is the frequency of the current in Hz, $\mu_0$ is the permeability of vacuum in $H \cdot m^{-1}$ and $\mu_r$ is the relative permeability of the material in $H \cdot m^{-1}$. For a copper wire with round cross section and an electric current with 30000 Hz frequency, the skin depth is about $4.2 \cdot 10^{-4}$ m or 0.42 mm. A wire thin enough to prevent ohmic losses due to the skin effect would not be able to withstand the several thousand amperes flowing through it when the capacitor is discharged. In order to increase the surface area two coil types were considered. One of them was an edge-wound coil made of flat, rectangular cross section wire the other one was a Bitter-type electromagnet. After careful consideration and consulting with experts at the national

High Magnetic Field Laboratory (NHMFL), it was decided that the superior mechanical stability and ease of assembly of the Bitter-type electromagnets make it the more suitable candidate. Bitter type electromagnets have a large surface to volume ratio, which makes them ideal for high frequency applications. On the other hand, they still have enough volume to efficiently dissipate heat and withstand the arising Lorentz forces.

In general, Bitter-type electromagnets consist of plates made of a highly conductive material stacked with layers of insulator disks. The disks are usually ring shaped, with a radial incision to disrupt the conductive path. Patterned holes are also cut into the disks to allow coolant to pass through the coil.

Due to the low duty cycle of the magnetic field and the intermittent operation of the apparatus, it was deemed unnecessary to include a liquid cooling system in the design of our device. It would have added unnecessary complexity and weight to the system at the cost of portability and modularity.

## 2.2 Construction of the electromagnets

C-shaped plates (Figure 2, left) were created of 0.41 mm thick copper-zirconium alloy sheets (a generous donation from the NHMFL). Insulator plates of the same dimensions were also cut out (Figure 2, right). Four 3 mm diameter holes were cut into the plates for the alignment pins used during the assembly process. These holes also perform as air flow channels, aiding in the cooling of the coils.

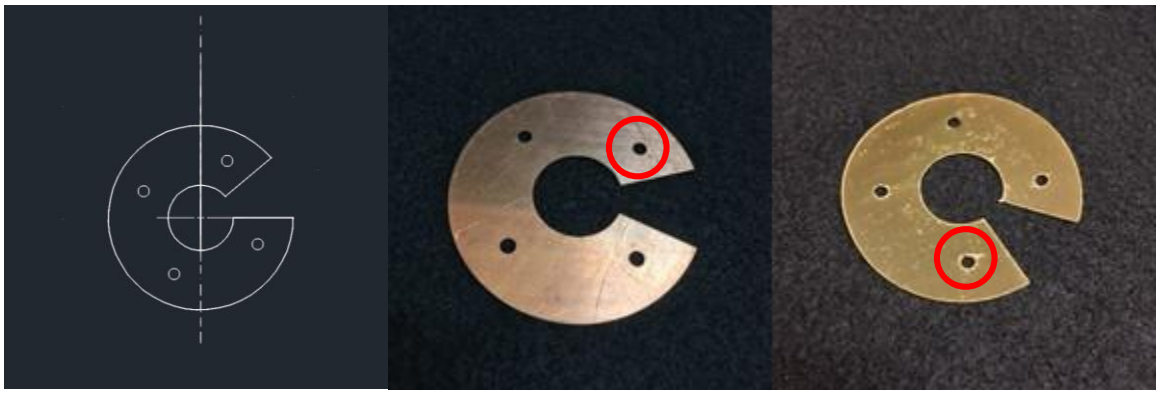

**Figure 2 C-shaped CuZr plate (left) and insulator plate (right)**

During the assembly four pins were used to align the stacked plates and keep them in place. To construct a helical conductive path, a conductive plate and an insulator plate were placed on top of each other, then the insulator was rotated 90 degrees and its end was passed through the gap in the copper plate, until the holes highlighted in Figure 2 overlapped. Then these units were stacked on the four-pin scaffolding, each rotated 90 degrees compared to the previous conductor-insulator plate pair. Four of these plate-pairs made a whole turn of the coil.

**Figure 3 A conductor-insulator plate pair, ready for assembly**

Ring shaped plates were also manufactured and used as spacers in the center of the coils. For better connectivity and mechanical strength, the stacked plates were sandwiched between two

copper plates held together by four threaded rods. The endplates were set to parallel and the distance between them was adjusted by tightening the nuts on the rods (Figure 4).

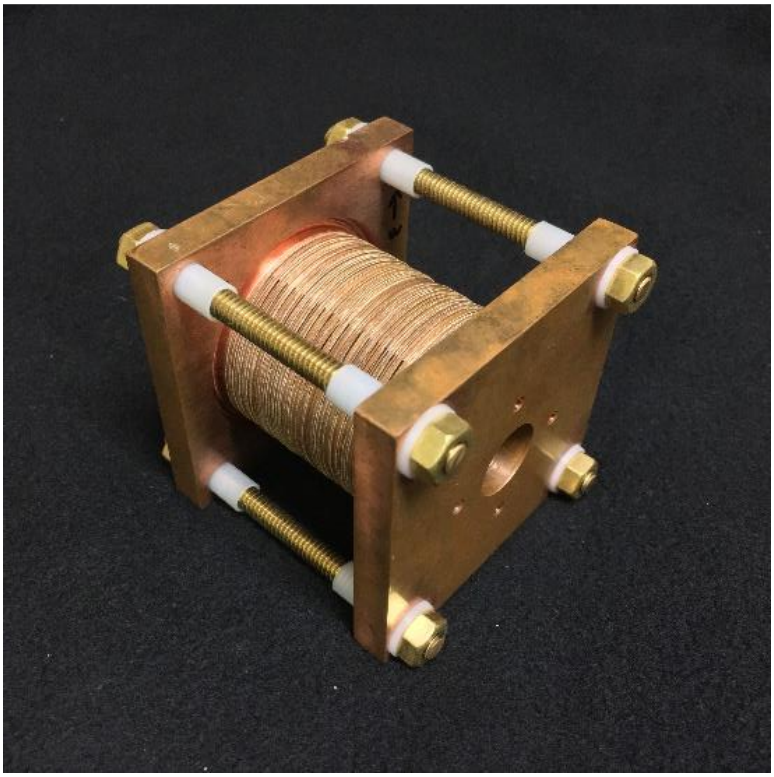

**Figure 4 The finished Bitter-type electromagnet**

Two variants of the coil were assembled. For both variants two half coils were assembled, separated by five spacers. Each of the half coils consisted of forty-three plate-pairs. One of the variants mimics a Helmholtz-coil. This means that the helicity of the half coils is identical and the magnetic field strength is highest at the center of the coil. The other variant mimics an anti-Helmholtz-coil, in which the helicity of the half coils is the opposite of each other's. This design generates a magnetic field with high magnetic field gradient, with the highest gradient in the center of the coil. Neither of these variants is a true Helmholtz or anti-Helmholtz-coil, since the distance between the half coils is not equal to the coil diameter.

To connect the electromagnets into the circuit, copper rails were fastened to the endplates. The coils were connected in series by the rails and covered by a plexiglass case as a safety precaution (Figure 5).

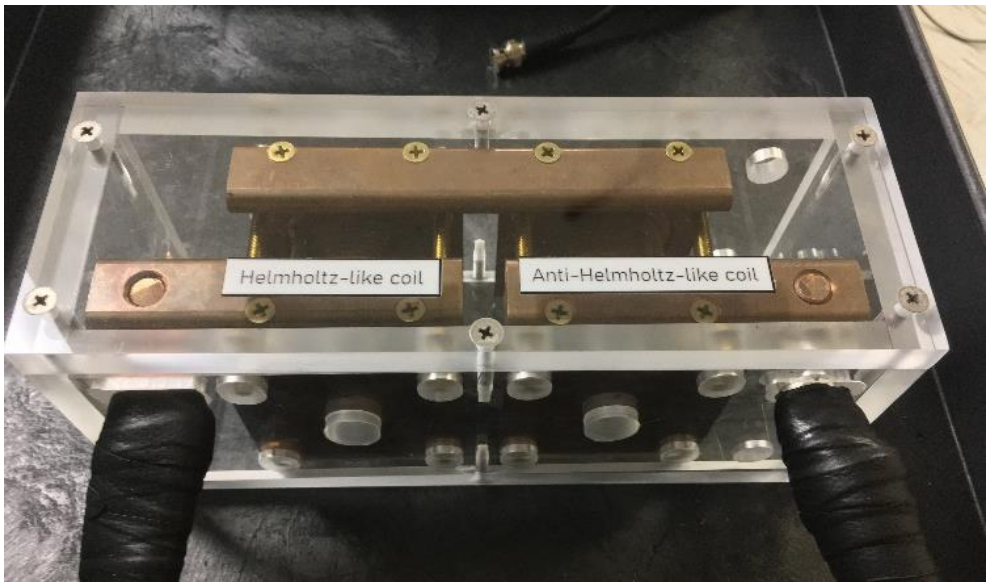


**Figure 5 The electromagnet installed on the instrument cart**

For additional safety, the high voltage cables close to the connections were wrapped in rubberized insulating tape.

# Chapter 3 - The resonant circuit

## 3.1 Rationale and design of the resonant circuit

To generate a magnetic pulse, a strong electric current pulse must flow through the electromagnet. To obtain the highest current possible, the Bitter-type electromagnets were used as the inductor in a resonant circuit. In theory, a resonant circuit consists of an inductor (which is a coil) and a capacitor. The discharge of the capacitor sends a pulse of electric current through the inductor, in which a magnetic field is induced. When the pulse stops, the magnetic field diminishes. This changing magnetic field induces electric current in the coil, which charges the capacitor. Without losses, this process is repeated indefinitely the circuit acts as a harmonic oscillator. However, since all conductors have finite conductivity and the connections of the parts are not without interface, there is always some resistance in the circuit. This resistance causes losses, mainly through heat generation. The heating power is proportional to the resistance and square of the current (3). These losses cause the system to lose energy over time. This loss of amplitude is called damping.

$$P \propto I^2 \cdot R \tag{3}$$

where $P$ is the power of heating, $I$ is the current and $R$ is the resistance of the heating element in question.

This oscillation however, happens only in a narrow frequency range. The oscillation and the increase of current carrying capability is the result in an apparent decrease of the circuit's impedance (4).

$$Z = R + i \cdot X \tag{4}$$

where $Z$ is the impedance, $R$ is the resistance of the circuit and $X$ is the reactance of the circuit. The impedance measures the overall limitations the circuit imposes on the flow of electric current. The first component of the impedance is the resistance of a circuit. It measures how much the circuit or a circuit element limits the flow of electric current. The second, imaginary term of the impedance is the reactance. The reactance measures how much the circuit or a circuit element opposes changes in the current or in the voltage, due to its capacitance or inductance. The capacitive reactance can be calculated the following way (5).

$$X_C = \frac{1}{2 \cdot \pi \cdot f \cdot C} \tag{5}$$

where $X_C$ is the capacitive reactance, $f$ is the frequency and $C$ is the capacitance of the circuit or circuit element. It can be seen that as the frequency increases, the capacitive reactance decreases. This decrease can be described with a hyperbolic curve.

The inductive reactance can be determined by using the following equation (6).

$$X_L = 2 \cdot \pi \cdot f \cdot L \tag{6}$$

where $X_L$ is the inductive reactance of the circuit or circuit element and $L$ is the inductance of the circuit or circuit element. The inductive reactance linearly increases with increasing frequency.

When the capacitive and inductive reactance are combined and plotted as a function of frequency, the curve shows a minimum at the resonance frequency. This means that at (and very near to) that frequency, the impedance of the circuit is lowest at the resonance frequency. Since at the resonance condition $X_C$ is equal to $X_L$, the resonance frequency can be easily calculated from the capacitance and inductance of the circuit (7).

$$f_{resonance} = \frac{1}{2 \cdot \pi \cdot \sqrt{C \cdot L}} \tag{7}$$

Otherwise, if the resonance frequency is known, the inductance of the circuit, which is largely contributed by the coils, can be determined (8).

$$L = \frac{1}{4 \cdot \pi^2 \cdot {f_{resonance}}^2 \cdot C} \quad (8)$$

In order to generate ultrasound by the agitation of magnetic nanoparticles, the frequency of the oscillatory motion of the nanoparticles needs to be in the 20000-30000 Hz regime. 20000 Hz is the lower limit of the ultrasonic frequency range and this frequency is also lower than the frequencies usually associated with magnetic hyperthermia (80000-100000 Hz). To adjust the resonance frequency of the circuit to be in this region, we chose a high frequency capacitor (Figure 6) with a capacitance value of 2.83 µF (microFarad, measured by a digital multimeter).

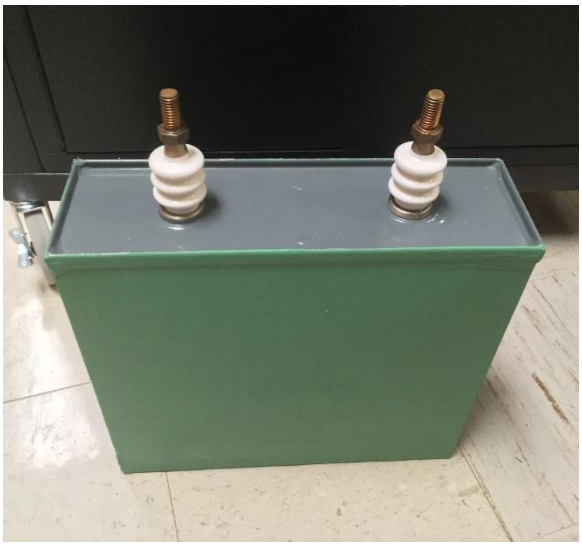

**Figure 6 High frequency capacitor**

The capacitor can be charged to a voltage between 500 and 10000 V with a CCPF-500-10P capacitor charger (from Lumina Power, Inc.). In order to prolong the lifetime of the capacitor, the default charging voltage is set to 6000 V.

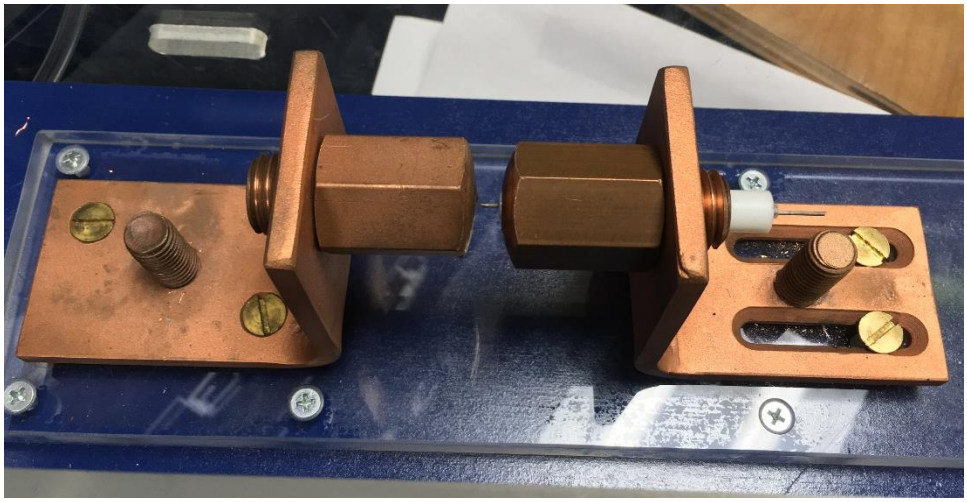

**Figure 7 Copper electrodes of the spark gap switch**

To trigger the discharge of the capacitor, a triggered spark gap switch was used. The switch is connected in series with the other circuit elements with braided cables rated for high voltage and high frequency. The main components of the switch are two copper electrodes with the gap between them large enough so that the potential difference between the electrodes cannot reach the breakdown threshold and no spontaneous discharge can occur. The breakdown voltage can be calculated by using Paschen's Law (9).

$$V_B = \frac{B \cdot p \cdot d}{ln(A \cdot p \cdot d) - ln\left[ln\left(1+\frac{1}{\gamma_{se}}\right)\right]} \tag{9}$$

where $V_B$ is the breakdown voltage, $A$ and $B$ are constants that depend on the gas in the spark gap, $p$ is the pressure of the gas and $\gamma_{se}$ is the secondary electron emission coefficient.

One of the two electrodes is solid copper, the other one has a bore through it. A Teflon sleeve with a glass capillary insert is placed into the bore. A tungsten pin is fed through the glass capillary so that the distance between the tip of the pin and the end of the solid electrode is about 3 mm (Figure 7). With the adjustment of the pin-electrode distance the breakdown threshold and the triggering accuracy can be controlled.

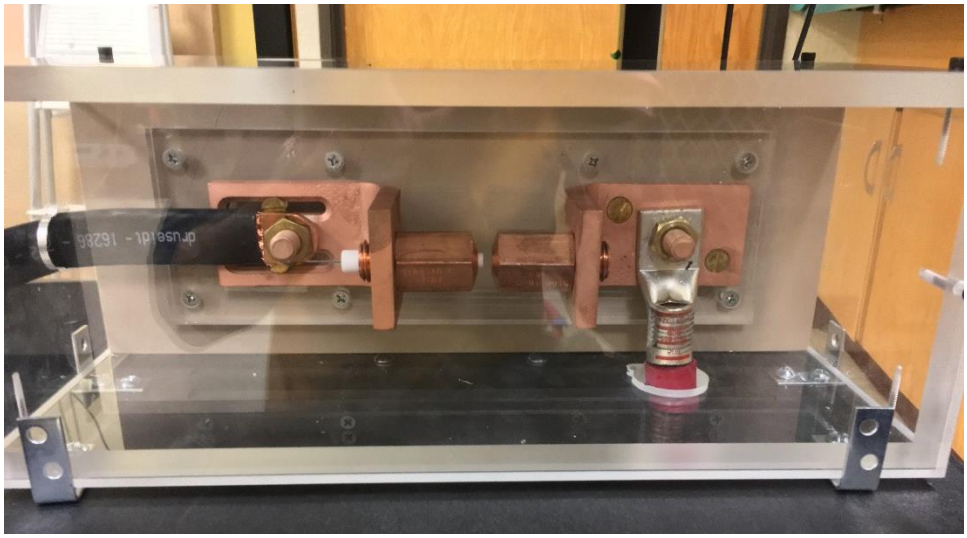

**Figure 8 The triggered spark gap switch installed on the instrument cart**

In order to trigger the discharge of the capacitor, the circuit must be closed. This is achieved by using an IGNITOR10 HV TRIGGER high voltage pulse generator (from Information Unlimited) with a 25 kV trigger transformer. When the pulse generator is turned on, the high voltage creates an electric spark between the electrodes, ionizing the gas in the spark gap. With the increase in the number of charged particles in the spark gap, the breakdown voltage is decrease so the potential difference between the plates of the capacitor is now high enough to spark over and the capacitor can be discharged. The circuit diagram of the resonant circuit and the charging circuit is shown in Figure 9. In order to protect the charger from feedback current, a voltage reversal circuit was implemented.

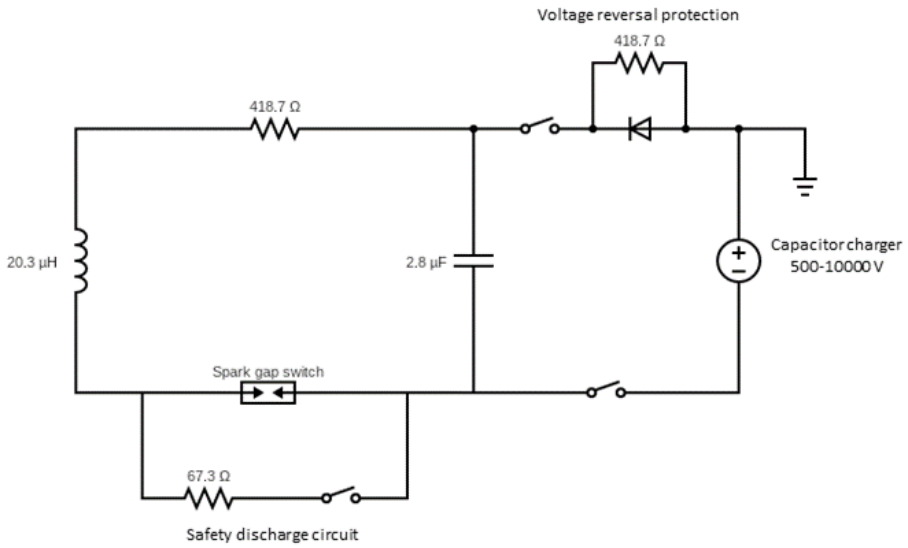


**Figure 9 Circuit diagram of the magnetic pulse generator (discharging circuit on the left, charging circuit on the right)**

As control switches, high voltage (10 kV) relays were used (G81A and G81B, from Gigavac). The switch in the safety discharge circuit is normally closed the other two switches are normally open. A safety discharge circuit with a 67.3 Ohm non-inductive resistor was built in, in order to avoid charge accumulation in the capacitor when the instrument is not in use. All resistors used are non-inductive ceramic resistors.

The instrument is assembled on a four-wheeled, heavy duty instrument cart. The control panel and the electromagnets are on the top level of the cart. The spark gap switch, the high voltage trigger spark generator and the optical isolator are located on the middle shelf of the cart that allows for easy access, but provides some protection for the sensitive electronics. The bottom, closed compartment contains the high voltage capacitor, the charger and most of the circuitry. All the elements in the charging, trigger and safety circuits are connected by high voltage cables rated for 25000 V. The high voltage cables of the discharge circuit are located in the end of the cart furthest from the operator.

## 3.2 Control system of the magnetic pulse generator

In order to reproducibly generate electromagnetic pulses, a controller with reliable output sequence was needed. As the main controller unit, a programmable logic controller (PLC) was chosen (SG2-20HT-D, from FactoryMation). This unit has eight DC input ports, four analog input ports and eight transistor output ports. The power source for the controller is a 24 V DC, 1.3 A power supply unit (10PS-24, from FactoryMation), which is an AC/DC converter with input voltage between 100 and 240 V. Two expansion modules were also installed. One of them has four DC input ports and four relay output ports (8ER-D, from FactoryMation), the other one has two 10-bit analog output channels (2 AO, from FactoryMation). The controller program is shown in Appendix 2. The sequence is as follows. First, the connection to ground is removed. Then, the safety discharge circuit's switch is opened and the charging circuit is engaged. The charger is turned on, the desired charging voltage is set and the charging of the capacitor begins. The charging level of the capacitor is continuously monitored and displayed on a voltmeter on the control panel. Once the target voltage is reached, the charger is turned off and the charging circuit is disengaged. A trigger pulse is sent to the high voltage trigger spark generator, to trigger the discharge of the capacitor. After the capacitor is discharged, the safety discharge circuit's switch is closed and connection to the ground is engaged.

Unfortunately, the rise time of the trigger signal generated by the PLC is not short enough to trigger the spark generator. In order to obtain an appropriate pulse form, an Arduino unit is built into the control panel. When the Arduino receives the signal from the PLC, it sends out a series of 5V rectangular pulses (A.3). This pulse sequence is able to act as a trigger for the spark generator and the series of electric arcs in the spark gap ensure the discharge of the capacitor. In order to protect the PLC panels from possible feedback current, an optical isolator is placed between the

PLC module and the spark generator. This isolator converts the trigger pulse into an optical signal, then converts it back to an electric signal. This allows for the transmission of the trigger signal without having electrical contact between the discharging circuit and the control panel. The isolator operates on two sets of three 1.5 V rechargeable batteries.

A small oscilloscope module was built into the control panel, to offer the option to monitor the waveform of the electromagnetic pulses. To obtain a signal, a current sensor (for example a Rogowski coil) can be connected via a BNC cable.

### 3.3 Operation of the instrument

For ease of operation, only the most necessary controls are exposed on the finished control panel (Figure 10). After connecting the instrument to the power outlet and to the ground in the laboratory, the user can turn on the instrument by turning the red switch to the right (as indicated by the arrows on the switch). This powers up the PLC, the Arduino module and the oscilloscope module. As the next step, the user should turn on the optical isolator and the trigger spark generator.


**Figure 10 User accessible controls on the pulsed magnetic field instrument (Left: main control panel, Center: trigger spark generator, Right: optical isolator)**

The trigger spark generator has multiple modes of operation (manual, continuous, remote). For this application, it should be set to the remote mode (rightmost position of the dial on the

currently installed spark generator). Once all the components are powered up, the sequence can be initiated by pulling up the green switch.

After the program has started, the instrument will discharge the capacitor and generate an electromagnetic pulse every 20 seconds. A few second before the discharge a red LED lights up in order to notify the user about the upcoming discharge. The operation can be interrupted any time by the user, by pushing down the green switch. This will connect the circuit to the ground and engage the safety discharge circuit. To change samples in the electromagnets, it is advised to interrupt the discharging sequence for the time the user might come into contact with exposed parts of the circuitry. When wanting to shut down the instrument, the user should push down the green and red buttons, turn off the optical isolator and the trigger spark generator, unplug the power cable from the insulator and disconnect the ground cable from the building's main ground. During storage the cables should be coiled up and hung on the designated hooks and the instrument cart's lower compartment doors should be locked.

# Chapter 4 - Experimental results

## 4.1 Determination of resonance frequency and inductance

The first experiment performed with the instrument was to determine the resonance frequency of the circuit. A Rogowski-coil was used as a current sensor and the electromagnetic pulse was recorded with an oscilloscope. The waveform was recorded nine times and the average of the values was taken to reduce noise. The resulting pulse waveform is shown in Figure 11.

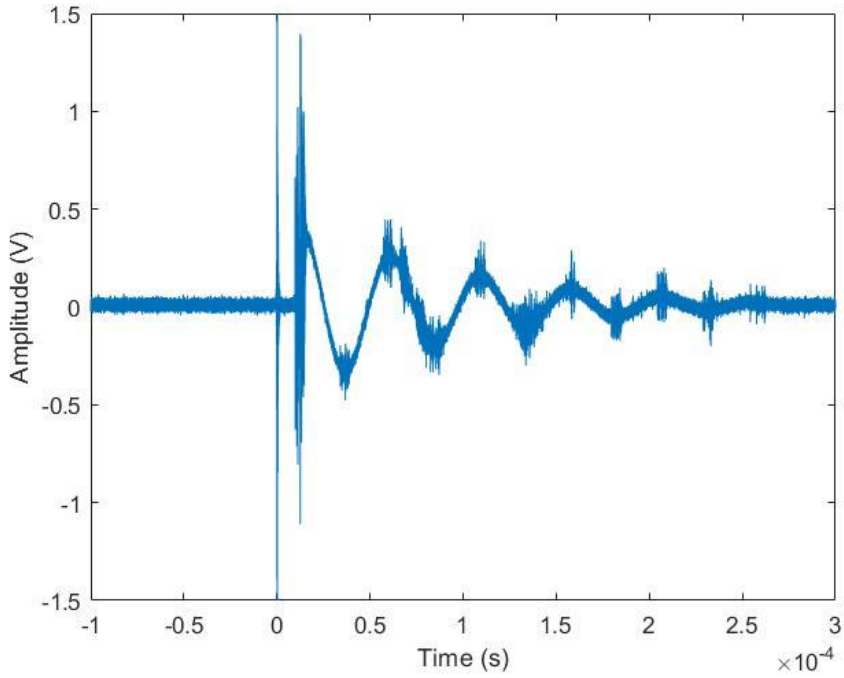


**Figure 11 Waveform of the electromagnetic pulse**

The initial, very sharp peak is caused by the high voltage trigger spark generator that we use to discharge the capacitor. To avoid misfires and ensure the triggering of the magnetic pulse, we apply a rapid succession of pulses and this causes the noise observable on the signal. The decay time of the pulse is about 250 μs. A Matlab code was written to process the data (A.1). The resonance frequency was determined by applying Fourier-transformation to the waveform data, converting it from time domain to frequency domain. The resonance frequency was found to be 21000 Hz (Figure 12).

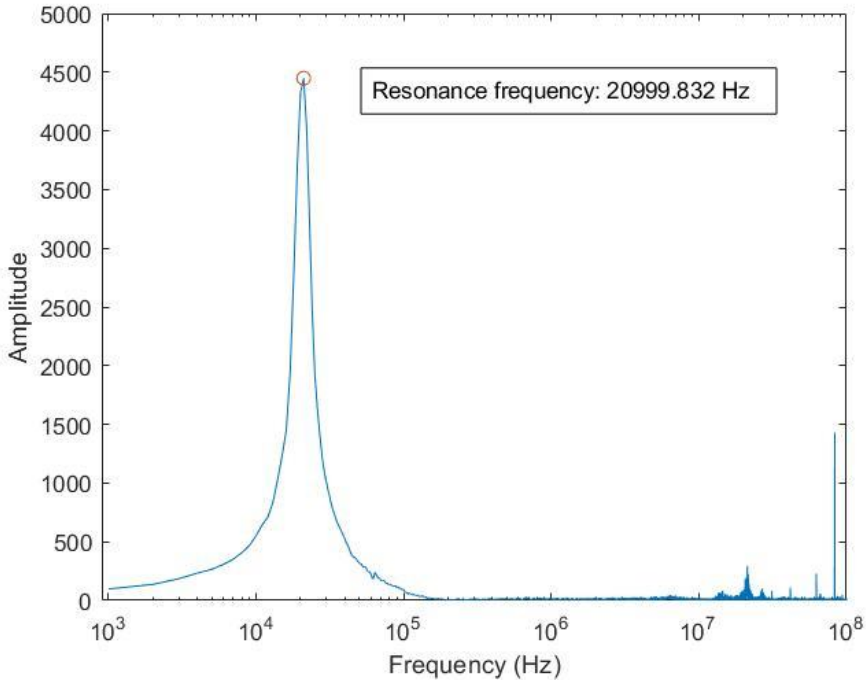


**Figure 12 Frequency spectrum of the electromagnetic pulse**

## 4.2 Determination of the coil pair's inductance

Once the resonance frequency of the circuit was known, the inductance of the coil pair could be calculated. In case of an ideal resonant circuit, where the only source of inductance is the inductor, equation (8) can be used to find the exact solution. In a real circuit, other circuit elements (such as cables and resistors) also contribute to the overall inductance of the circuit. However, in this work we assumed that the inductance of the coil pair is so much higher than that of the other elements that it can be taken as the only source of inductance. With a resonant frequency of 21000 Hz and a capacitance of 2.83 µF, the inductance of the coil pair was found to be 20.3 µH.

## 4.3 Visualization of the magnetic field

Another aspect of interest is the magnetic field strength profile of the coils along their axis. In case of the Helmholtz-like coil, we expect the highest magnetic field strength to be at the center of the coil. This is because the helicities of the two half coils are the same so the direction of the induced magnetic field will be identical. If the magnetic field strength profiles of the half coils are modelled with a Gaussian function, in case of the Helmholtz-like coil, both bell curves will be positive, constructively combining at the center of the coil. On the other hand, the magnetic field strength of the anti-Helmholtz-like coil is expected to be zero or close to zero in the center. The helicities of the two half coils in the anti-Helmholtz-like electromagnet are opposites of each other. Therefore, the induced magnetic field vectors point in opposite directions. This means that the one of the Gaussian curves describing the magnetic field strength along the axis of the coil will be positive, the other will be negative. Therefore, the magnetic forces should cancel out each other, where they overlap.

The visualization of the magnetic fields was first attempted by using fine iron powder (5-9 μm, 99.9%, from Strem Chemicals, Inc.) suspended in glycerol (from Fischer biotech). The same kind of adherent cell culture tubes which the electromagnets were designed to fit were used as sample vials. Iron powder was dispersed in glycerol and the inner wall of the cell culture tube was coated with the suspension. The tube was placed into the electromagnet and was exposed to a single magnetic pulse. One pulse did not prove to be enough to appreciably move the iron particles. Therefore a new sample was prepared and exposed to ten consecutive pulses (Figure 13).

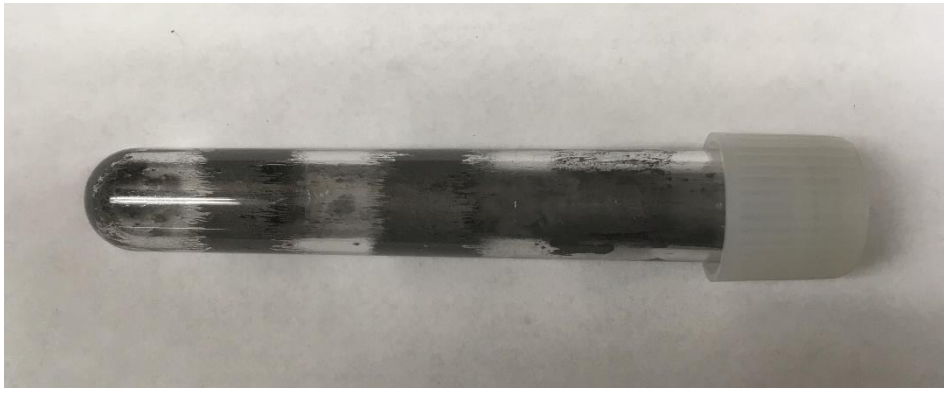

**Figure 13 Cell culture tube with iron powder in glycerol suspension (After ten magnetic pulses in the anti-Helmholtz-like electromagnet.)**

It can be clearly seen that the iron particles moved along the magnetic field gradient. However, the reproducibility of this method was questionable, the tubes could not be cleaned properly and the wide bands did not provide a high enough resolution to claim this method as suitable imaging technique.

In order to obtain a higher resolution image, a magnetic field viewing film was purchased (from CMS Magnetics). The film is a polymer sheet coated with microcapsules, containing magnetic nanoparticles in an oil suspension. Unfortunately, the manufacturer did not provide any information about the nanoparticles. We assume that the nanoparticles have anisotropic shape, because when they are aligned due to an external magnetic field, the reflection characteristics of the film change.

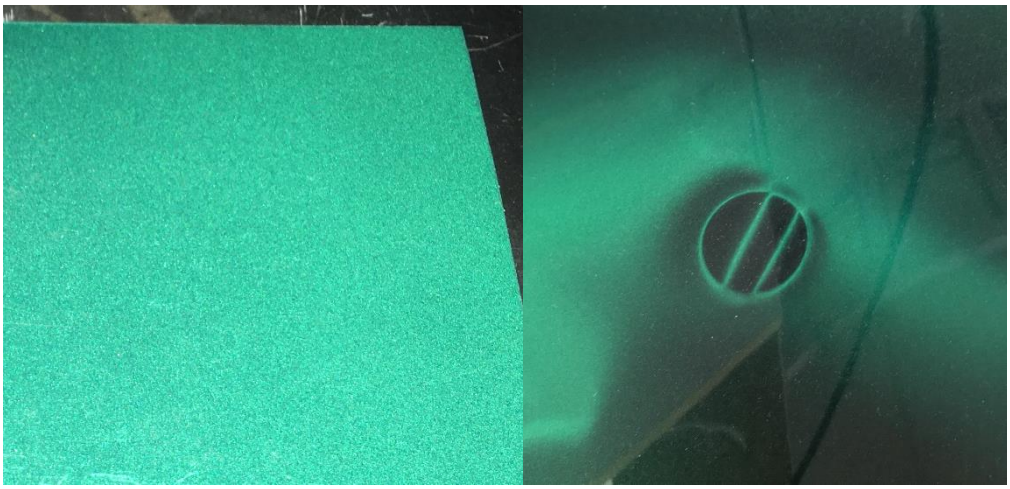

**Figure 14 Magnetic field viewing film**
**(Left: native color, Right: with multipole magnetized magnet placed underneath it)**

When the magnetic field lines are perpendicular to the plane defined by the film, the reflectivity decreases and the color of the film appears darker. When the field lines are parallel to the sheet, the reflectivity increases. Therefore, the color appears lighter (Figure 14). The native green color of the film is due to a dye added to the oil found in the microcapsules. The obtained magnetic field image is permanent unless another external field changes it. Since the Bitter-type electromagnets of our instrument are operated in pulsed mode, the spatial profile of the magnetic field strength can be recorded without the fear of overwriting or destroying it by removing the film from the electromagnets between pulses. These properties make this type of magnetic field viewing film a viable tool for magnetic field visualization.

In order to record the magnetic field profile of the electromagnets, the film was rolled up and inserted into the Bitter-coils' bores. The capacitor was discharged once, exposing the magnetic field viewing film to a single magnetic pulse. After the application of the magnetic pulse, the instrument was turned off. The film was then removed, unrolled and photographed (Figure 15).

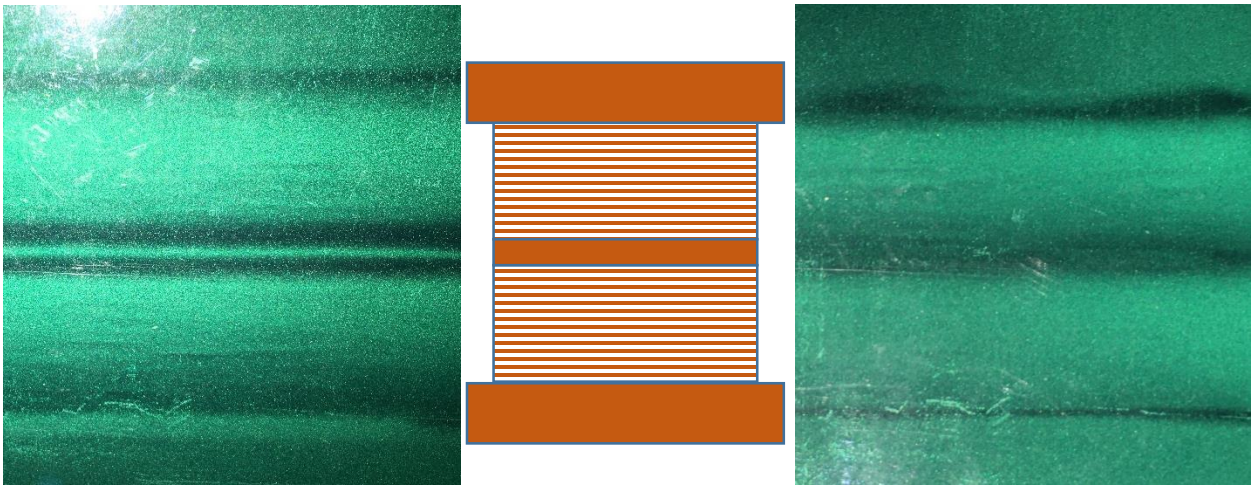

**Figure 15 Magnetic field profile images of the coils (Left: Helmholtz-like coil, Right: anti-Helmholtz-like coil, Center: schematic drawing of the coils for reference)**

When the film was exposed to the magnetic pulse, the encapsulated nanoparticles were aligned in a distinctive pattern. By drawing an analogy between the field line distribution of an electromagnetic coil and a static bar magnet, the patterns can be easily explained. Inside the two half-coils, where the magnetic field lines are supposed to be parallel to the axis of the coil, the color of the film became lighter, indicating that indeed, the direction of the magnetic field is parallel to the plane of the magnetic field viewing film. The region between the two half-coils can be modelled by two magnetic poles brought into close proximity of each other (Figure 16). In case of the Helmholtz-like coil, the helicities of the two half-coils are identical. Due to this, the direction of the generated magnetic fields is the same and at the center of the electromagnet, the "north pole" of one of the half-coils is close to the "south pole" of the other half-coil. In case of the anti-Helmholtz-like coil, the helicities of the two half-coils are the opposites of each other thus the direction of generated magnetic fields are opposites, as well. This orientation is analogous to the system in which two static magnets are positioned with the same poles facing each other (north-north, south-south).

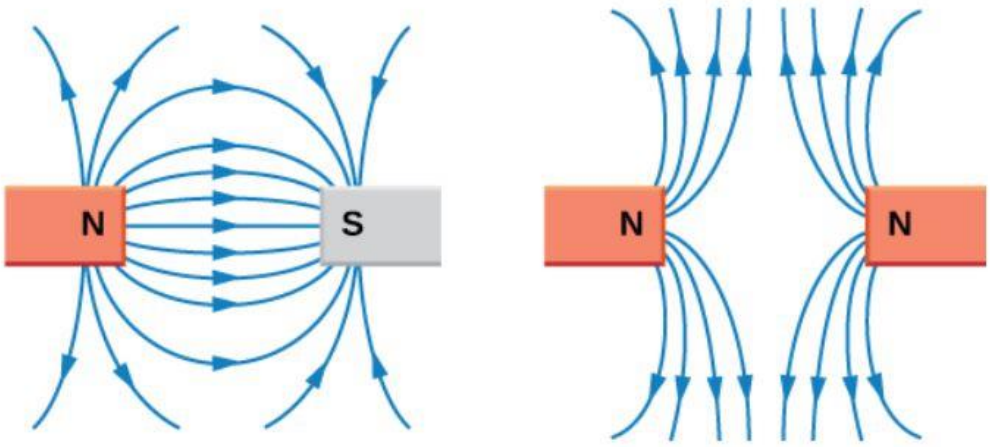


**Figure 16 Magnetic poles in close proximity[26]**

In the middle region of the magnetic field image taken of the Helmholtz-like electromagnet, two dark lines can be seen with a lighter line between them. Since the magnetic field viewing film is rolled up and placed inside the electromagnets, the magnetic field lines imaged are the ones that lie close to the center line of the coils, not the ones that extend out into the space outside the coils. The dark lines can be attributed to those magnetic field lines originating near the ends of the half-coils that are close to perpendicular to the axis of the coil. The nanoparticles in the regions where the field lines are perpendicular are aligned in a way that decreases the reflectivity of the film. The single, lighter line is caused by the alignment of the nanoparticles caused by a magnetic field between the two half-coils that is parallel to the axis of the coil and the film.

When the magnetic field image of the anti-Helmholtz-like coil is examined, a single, more diffuse dark band can be seen. This pattern can be explained by the lack of parallel magnetic field lines and the higher density of lines perpendicular to the coil and the magnetic field viewing film.

## 4.4 Prospects and plans for the pulsed magnetic field instrument

There is an ongoing cooperation between our research group and Professor Ryan Rafferty's research group, under a grant provided by the Johnson Cancer Research Center. In the research undertaken by the two groups magnetic pulse aided drug delivery mechanisms will be investigated. The instrument detailed in this thesis will be used to perform triggered drug release experiments on magneto liposomes, as well as drug internalization studies and cell viability assays on adherent cell cultures. Since our laboratory is not suitable for the sterile work required in microbiology and the cell cultures can be sensitive to the change of environment, the joint work has been slow. However, the instrument cart can be transported to Professor Rafferty's laboratory to perform the experiments there, thus opening up a path to a more fruitful cooperation. By using the cell culture tubes mentioned in the previous chapter, adherent cell lines can be brought into contact with a solution containing magnetic nanoparticles, drug loaded liposomes or drug loaded magneto liposomes, then exposed to a pulsed magnetic field. One side of the tubes being flat, microscope images of the cell culture can be taken before and after the treatment. Comparing the cells before and after the application of the magnetic pulses will help us understand how the magnetic field enhances drug internalization and release, thus aiding us in the design of more efficient drug delivery systems.

# Chapter 5 - Magnetic hyperthermia with rotating magnetic field

## 5.1 Nested Helmholtz-coil pair design for rotating magnetic field generation

Magnetic hyperthermia is used as a treatment method, as well as a means of triggering drug release from liposomes. In order to improve the existing methods, two experimental setups were constructed for the generation of a rotating magnetic field.

In the first set of experiment two perpendicular nested Helmholtz-coils were combined to produce a rotating magnetic field. In the experiments a pair of edge-wound Helmholtz coils was used. Edge wound coils have a higher surface area that helps to minimize the losses due to the skin effect at high frequency.

A smaller coil was nested in a larger outer coil in a way that their main axes of the coils were perpendicular to each other. For increased durability and easier mounting, the coils were covered with a plexiglass casing (Figure 17).

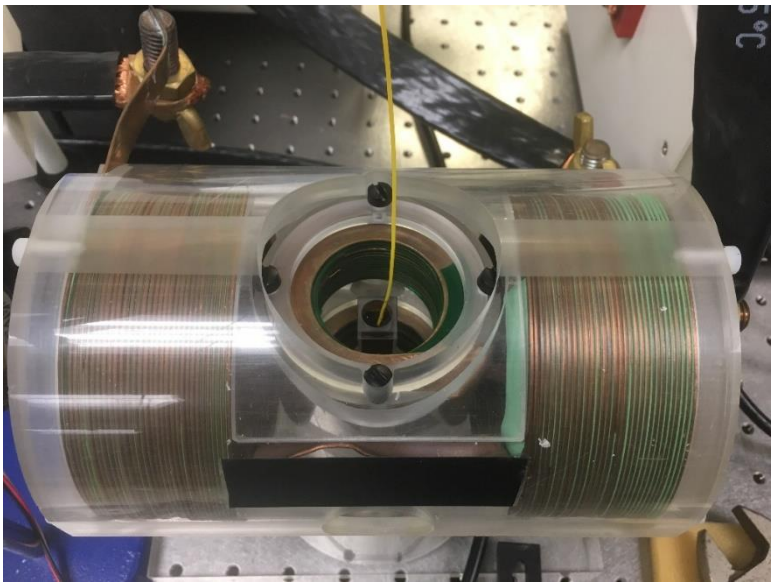

**Figure 17 A magnetic nanoparticle sample inserted into the nested Helmholtz coils (The yellow line is a fiber optic temperature sensor.)**

Each coil had a separate diving circuit that consisted of a waveform amplifier and capacitor(s). The capacitors (2.5 µF for the smaller inner coil, 0.025 µF for the larger outer coil) and the coils were connected in series, thus creating a resonant circuit (Figure 18). The maximum field strength can be achieved by using alternating current with frequency equal to the resonance frequency of the circuit. In the heating experiments, the sinusoidal driving signals were generated by a dual channel function generator, while during the frequency response test, the output of a lock-in amplifier (500 kHz, dual phase, digital signal processing) was used. In this arrangement the coils were capable of generating stationary, alternating or rotating magnetic fields, depending on the characteristics of the driving signals. Rogowski coil current sensors made in the research group were used to monitor the high frequency current. The signal of this type sensor is linearly proportional to the current that induces it.[27] During the frequency response tests, the high frequency voltage signal induced in the sensor was detected by a lock-in amplifier, while during the magnetic heating experiments a digital oscilloscope was used to monitor the current.

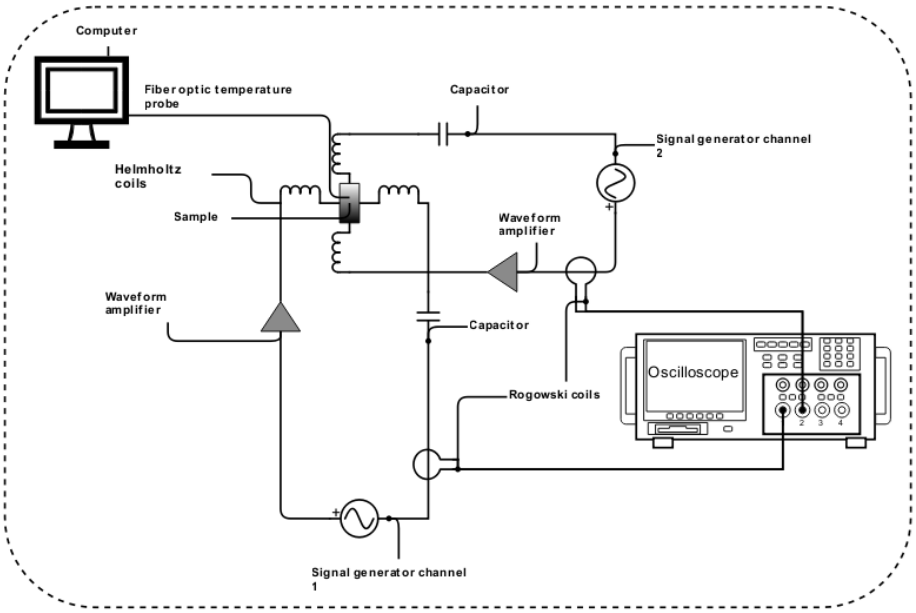


**Figure 18 Schematic diagram of the experimental setup used in the magnetic heating experiments**

## 5.2 Frequency response tests of the nested Helmholtz-coil system

In order to generate a perfectly circular, rotating magnetic field, the frequency and the amplitude of the AMF in the coils must be identical and the phase of the signals must be shifted by $\pi/2$. To reach the highest field strength possible, this frequency should be at or close to the resonant frequency of the circuits, the determination of which is done by the so-called frequency response test. The applied frequency was changed in the range between 10000 Hz and 100000 Hz, while monitoring the current flowing through the circuits. For this purpose, a LabVIEW program was written to communicate with a lock in detection system. Because the same coil was used to measure the current flowing in the circuit no data correction was necessary.

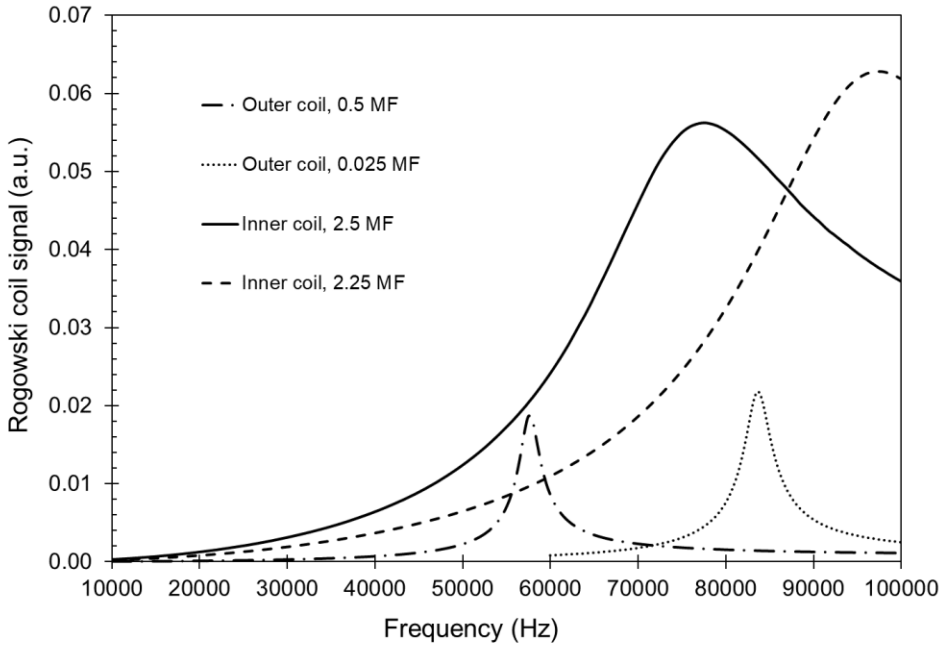


**Figure 19 The result of the frequency response test**
**(The different dashed lines indicate different capacitance values in the circuit.)**

The experimental setup was assembled in several ways, changing the capacitors in the circuit. As shown in Figure 19, the resonance frequency can be easily tuned by changing the

capacitance. The heating effect of nanoparticles exponentially increases with AMF frequency. Therefore, we wanted to use the highest frequency possible in the below-100000 Hz regime to avoid direct tissue heating. Since the maximum current peaks of the outer coil were much smaller and narrower than the peaks of the inner coil, it was more important to match the resonant frequency of the outer coil's circuit. For this reason, we chose the AMF frequency in our later experiments to be 83650 Hz. The significant broadening of the current peaks of the inner coil's circuit can possibly be attributed to an increased resistance of the system arising at electrical connections, or from the heating of the components.

### 5.3 Heating of magnetic nanoparticles in the rotating magnetic field of the nested Helmholtz coils

3.00 mL of an Iron-oxide nanoparticle-water dispersion (~20 nm, ferrofluid2 w%, EMG 607 from FerroTec) was placed in a quartz cuvette into the central air gap of the coils. The initial temperature of the sample was set to 21.5 ± 0.1 ºC. The driving signal's frequency was set to the determined resonant frequency of the coils (83650 Hz) and the phase delay between the sine waves driving the separate circuits was set to $\pi/2$. The induced magnetic field of the coils depends on the coil diameter and the number of turns. Therefore, the driving signal of the coils had to be changed independently. The voltage range from 0.0 V to 5.0 V was scanned in 0.5 V increments. The heating capability of the individual coils was tested, as well as the heating capability of an elliptically rotating magnetic field. The rotating field was generated by combining the alternating magnetic fields of the two coils. The corresponding signal from the Rogowski coil was then recorded. A fiber optic temperature probe (borrowed from the Department of Veterinary Medicine, through Professor Santosh Aryal) was immersed into the sample and its response was analyzed by a fiber optic signal conditioner connected to a computer. At each voltage, temperature data was

collected for approximately ten minutes. The accumulated data was processed with Matlab, to find the initial slope of the heating curve (A.3). During this experiment our goal was to show that the heating effect of a rotating magnetic field is not simply the sum of the heating effects of the individual coils, but a synergic interaction exists. Furthermore, we wanted to find the appropriate driving signal amplitudes for each of the coils, to gain the highest magnetic field strength possible. Finally, we wanted to use our device to determine the specific absorption rate (SAR) of nanoparticles.

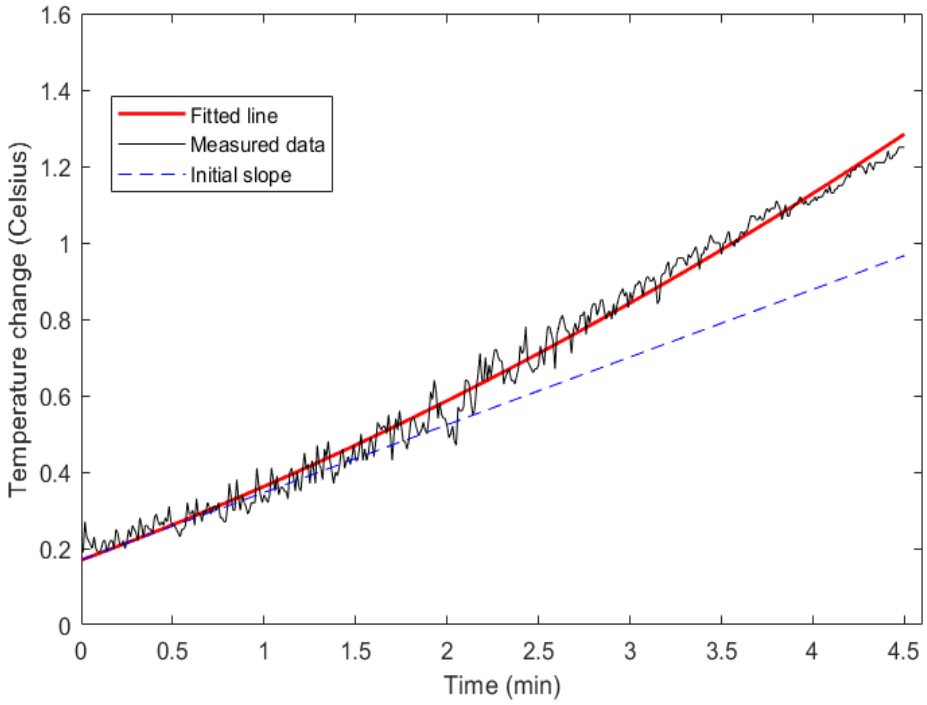


**Figure 20 Heating curve of Iron-oxide nanoparticles with fitted polynomial and initial slope line (obtained with nested Helmholtz-coil arrangement)**

The heating efficiency of magnetic nanoparticles is often characterized by their SAR value. The determination of this value can be done in a variety of ways[28], of which we intended to use the initial slope method[29]. A typical heating curve can be seen in Figure 20. The graph shows the temperature rise of the sample caused by the magnetic field (4.5 V voltage applied to both coils).

During data processing, the measured initial temperature was subtracted from all data points. Furthermore, to reduce the effect of internal and external heat transfer, the initial induction period (120 seconds) and all data points above 450 seconds were removed. After these corrections, the data was fitted with a second order polynomial (Figure 20). The initial slope was calculated as the slope of the polynomial at the first corrected data point. The initial slope values were then plotted as a function of the applied driving voltage (Figure 21).

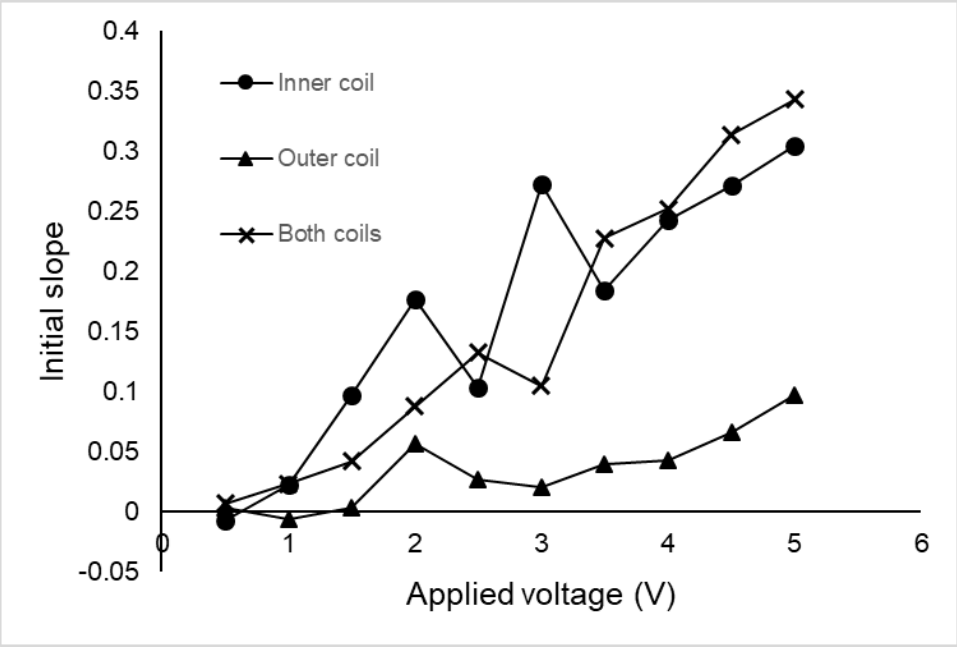


**Figure 21 The calculated initial slope values at different driving voltages**

It can be seen that by using higher driving voltages, the heating rate of the magnetic nanoparticles in the sample can be increased. However, with the nested Helmholtz-coil pair setup, it was not possible to achieve the same heating efficiency with both coils. Based on the exponential increase of the sample's temperature it was also suspected that the temperature increase was not caused by only the magnetic heating of the nanoparticles, but some other effect.

It was possible that the coils not only generated heat by magnetic effects, but through radiative heat transfer. To test this hypothesis, the experiment was repeated with distilled water as sample. The results confirmed our hypothesis. There was little to no difference between the temperature change of the nanoparticle and water samples (Figure 22).

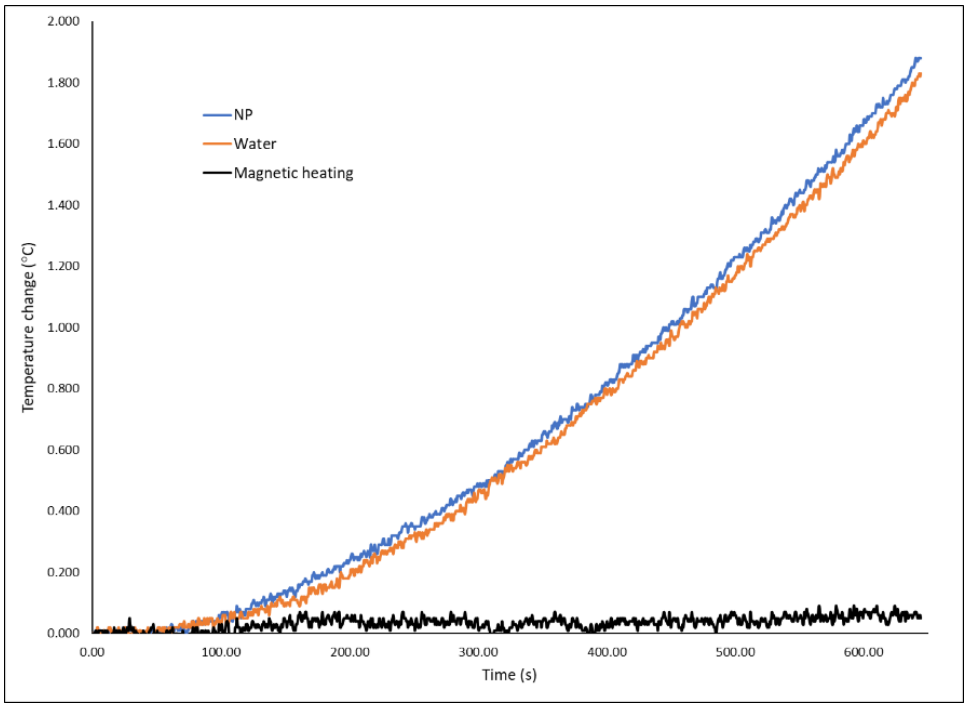


**Figure 22 The temperature changes of Iron-oxide nanoparticles dispersed in water (blue line) and distilled water (orange line) when exposed to magnetic field**

To determine where the heat was generated, thermal images were taken of the coils. An IR camera was borrowed from the Department of Veterinary Medicine with the help of Professor Santosh Aryal.

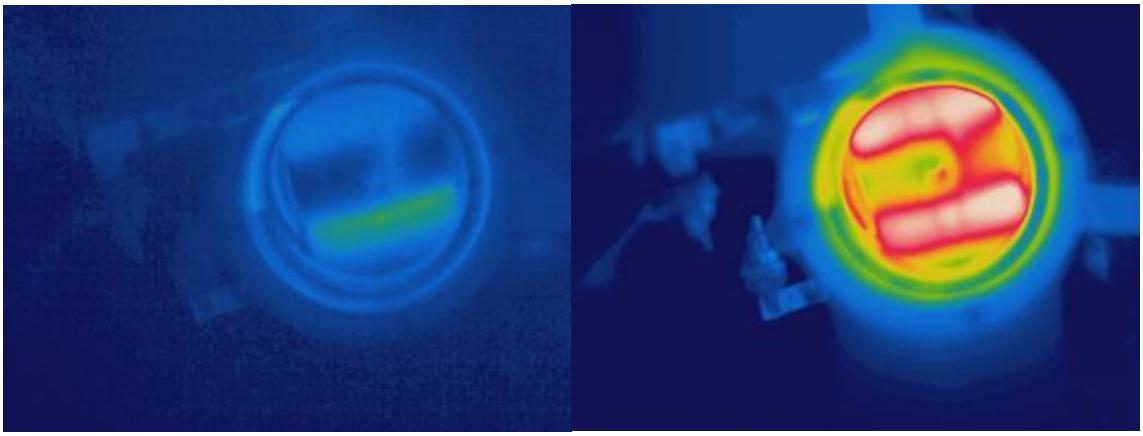

**Figure 23 Thermal images of the coils.**
**(Left: before the experiment, Right: after the experiment)**

It was shown that under operation, the inner coil's material increased from room temperature up to 70 °C. This may have been caused by a flaw in the coil design. The inner coil was capable of generating an alternating magnetic field that can induce magnetic hyperthermia. However, it shielded the sample from the magnetic field of the outer coil. The outer coil acted as an inductive heater on the inner coil, increasing its temperature and that was where the radiative heat came from. With this coil pair, this effect could not be eliminated. Therefore, we designed and constructed a new coil pair, in which the coils were still perpendicular but did not overlap.

The nested Helmholtz-coil pair arrangement can still be used in pulsed magnetic field generation, but due to the heating, it cannot be operated continuously.

## 5.4 3D printed coil design for rotating magnetic field generation

In order to eliminate the problems arising from a nested coil pair system, a new coil arrangement was designed. In the new installation, the spools for the perpendicular half coils were attached to a cuvette holder (Figure 24). This manifold was then 3D printed of PLA polymer at the KSU ITS Media Development Center.

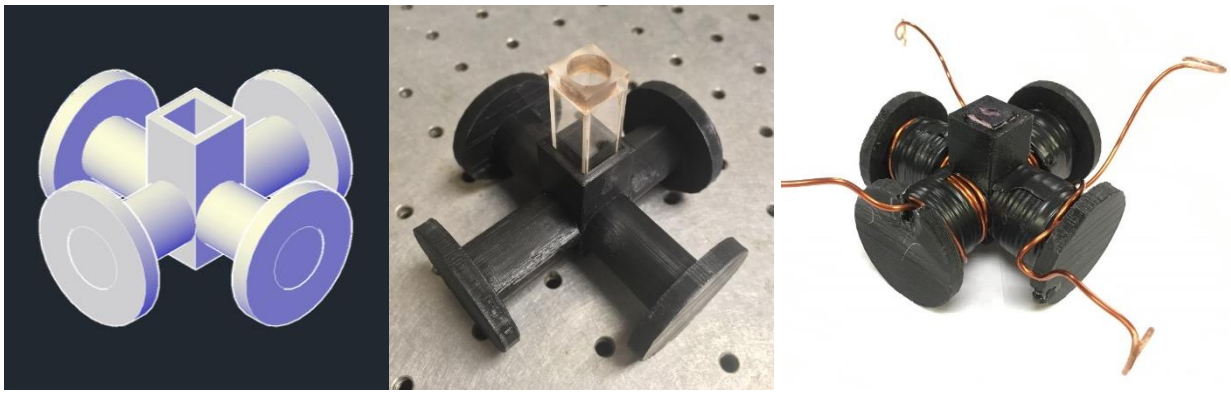

**Figure 24 Coil design for rotating magnetic field generation (Left: AutoCAD design of the coil base, Center: the 3D printed coil base, Right: the finished coil pair)**

Round cross section copper wire was then wound on the spools to create two perpendicular Helmholtz-coils. To generate magnetic fields, the same circuit was used as with the nested Helmholtz-coil pair system. The same Iron-oxide nanoparticle dispersion was used as a sample as in the previous experiments. The temperature of the sample was monitored and plotted as a function of time.

It was found that the background heating effect of the coils was still present. To minimize the heat-transfer between the coils and the sample, a closed cell Styrofoam insulator insert was made. The sample vial was changed from a cuvette to an NMR tube and the sample amount was reduced to 300 µL. To eliminate the background heating during the data processing, the heating

curves of the nanoparticle sample and distilled water were recorded under the same conditions and the water background was subtracted.

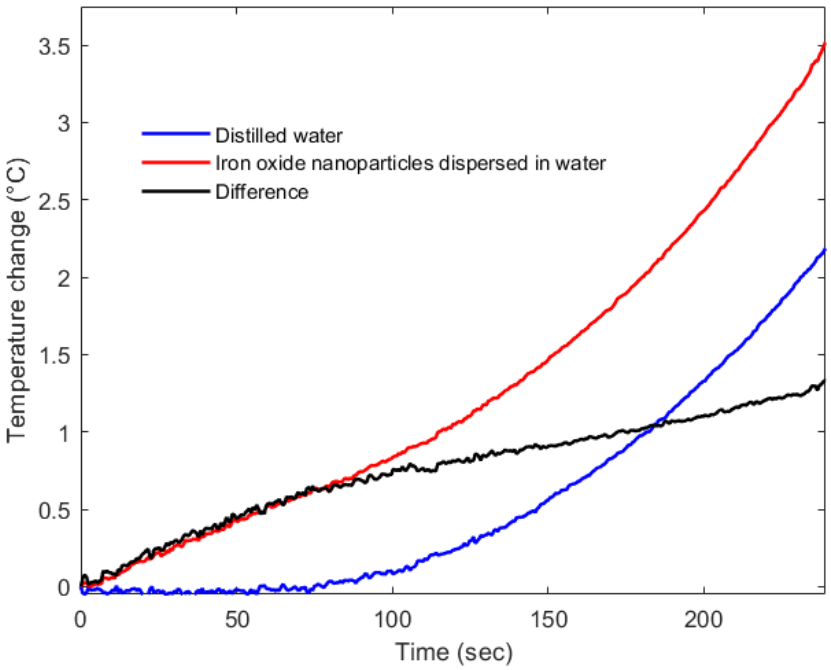


**Figure 25 Heating curves produced by the perpendicular solenoid system**

The difference curve between the sample's and the water background's heating curves is in good agreement with similar curves found in literature[29]; thus it can be said that it describes the heating effect of the magnetic nanoparticles exposed to the magnetic field.

The background corrected heating curve was fitted with a second order polynomial and the initial slope was calculated (Figure 26). The heating curves of the alternating field and the rotating field modes of the setup were also compared (Figure 27). It was found that when the perpendicular solenoid coils system was operated in the rotating field generation mode, its heating efficiency was higher than that of its alternating magnetic field mode.

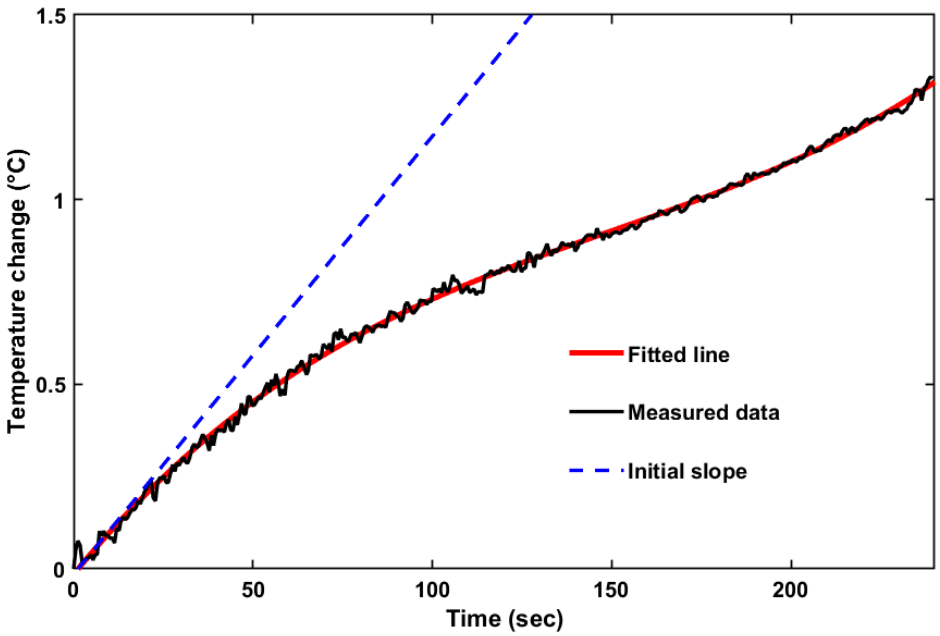


**Figure 26 Heating curve of Iron-oxide nanoparticles with fitted polynomial and initial slope line (obtained with perpendicular solenoids arrangement)**

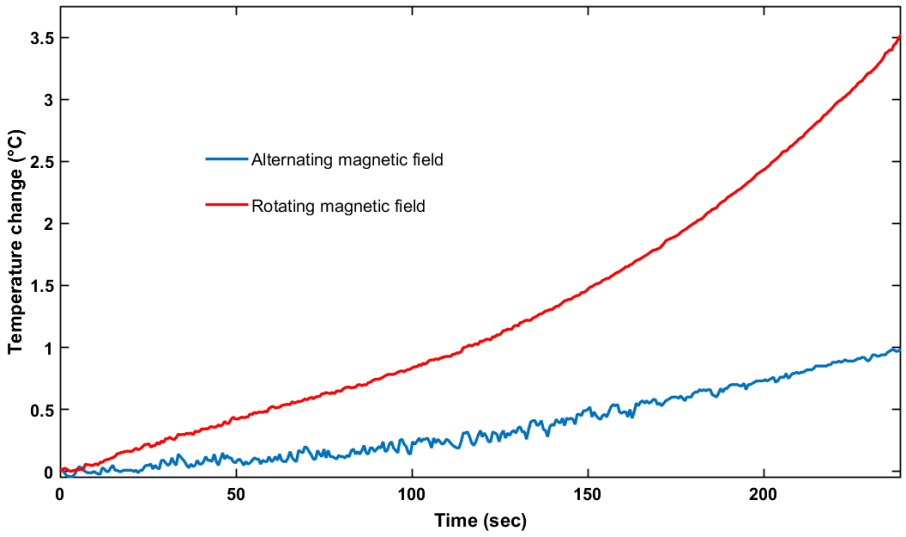


**Figure 27 Heating curve comparison between the alternating and the rotating magnetic field of the perpendicular solenoid arrangement (before background correction)**

In order to determine whether the increase in heating efficiency is a result of the rotating field or the increased magnetic field strength due to the simultaneous operation of both coils, the phase difference between the driving signals was changed. The phase difference was adjusted between 0 (completely in phase) and π (completely out of phase), in $\frac{\pi}{8}$ increments (Figure 28).

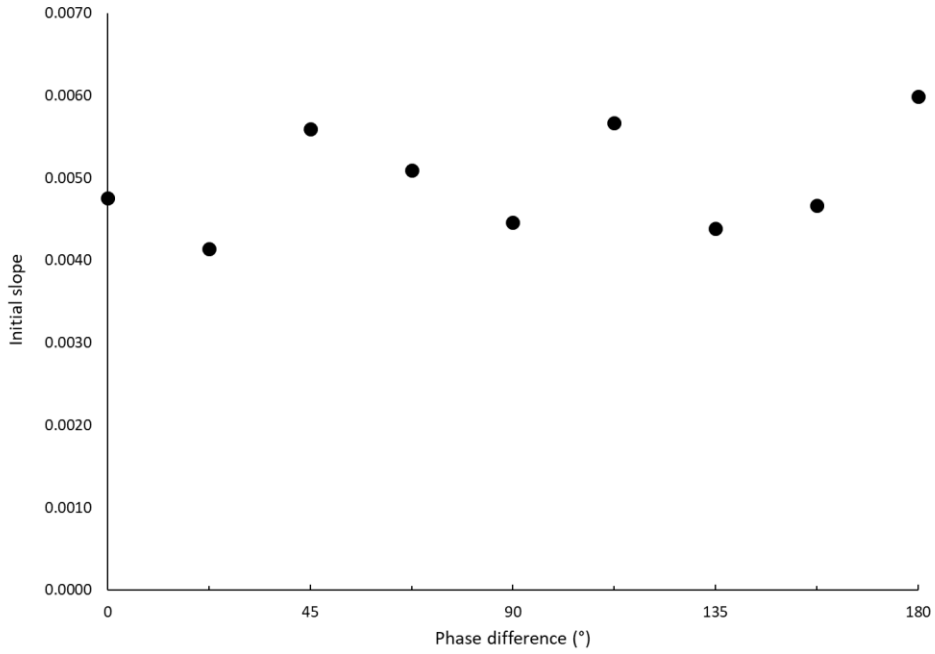


**Figure 28 Heating efficiency of magnetic fields with different ellipticity**

It was found that there is little to no difference between the heating efficiency of magnetic fields with different ellipticity. It can be concluded that in our experiments and with our experimental setup, there was no difference between the heating efficiency of the alternating and rotating magnetic fields.

We presume that order to completely eliminate the heating effect, the coils must be cooled by a liquid cooling system. The implementation of such a cooling system was not feasible in the work currently discussed.

# Chapter 6 - Conclusion

In this thesis the methods of magnetic field assisted drug delivery are presented, with focus on magnetic hyperthermia and the application of pulsed magnetic fields.

An instrument capable of generating pulsed magnetic fields with two different magnetic field profiles was constructed. The instrument is portable, facilitating further cooperation between research groups investigating areas where pulsed magnetic fields are required. The spatial profile of the generated magnetic fields was described. The details of the construction were shown. The strength of the magnetic field is yet to be determined, but the instrument is ready for cell line experiments and qualitative measurements.

Two electromagnet designs are described in this thesis. One of them is a nested Helmholtz-coil pair setup, which was used to evaluate the difference between the heating efficiency of alternating and rotating magnetic fields. The resonant frequency of the circuit was determined. An experimental method for magnetic hyperthermia experiments was designed and used to determine the heating capability of various magnetic fields. Unfortunately, this coil design did not prove to be suitable for continuous operation due to the heating of the coil material.

In order to address this issue, a new coil system design was implemented. A polymer base with two perpendicular spool pairs was designed. The base was 3D printed and copper wire was wound on the spools to create two perpendicular Helmholtz-coils. The heating efficiency of the new coil arrangement was evaluated in both alternating and rotating field generating mode.

When both of the coils were operated, generating a rotating magnetic field, the heating efficiency was much larger than the individual coil's alternating magnetic field's heating efficiency. However, when investigating the effect of the magnetic field's ellipticity on the heating efficiency, it was found that, with our experimental setup, the differences were negligible. Without

temperature control of the coils, the background heating effect cannot be sufficiently separated from the magnetic heating.

# References


1. Zverev, V. I.; Pyatakov, A. P.; Shtil, A. A.; Tishin, A. M., Novel applications of magnetic materials and technologies for medicine. *Journal of Magnetism and Magnetic Materials* **2018,** *459*, 182-186.

2. Wong, W.; Gan, W. L.; Liu, N.; Lew, W. S., Magneto-actuated cell apoptosis by biaxial pulsed magnetic field. *Scientific Reports* **2017,** *7* (1), 10919.

3. Chang, D.; Lim, M.; Goos, J.; Qiao, R.; Ng, Y. Y.; Mansfeld, F. M.; Jackson, M.; Davis, T. P.; Kavallaris, M., Biologically Targeted Magnetic Hyperthermia: Potential and Limitations. *Frontiers in Pharmacology* **2018,** *9*, 831.

4. Egolf, P. W.; Shamsudhin, N.; Pané, S.; Vuarnoz, D.; Pokki, J.; Pawlowski, A.-G.; Tsague, P.; de Marco, B.; Bovy, W.; Tucev, S.; Ansari, M. H. D.; Nelson, B. J., Hyperthermia with rotating magnetic nanowires inducing heat into tumor by fluid friction. *Journal of Applied Physics* **2016,** *120* (6), 064304.

5. Hatamie, S.; Parseh, B.; Ahadian, M. M.; Naghdabadi, F.; Saber, R.; Soleimani, M., Heat transfer of PEGylated cobalt ferrite nanofluids for magnetic fluid hyperthermia therapy: In vitro cellular study. *Journal of Magnetism and Magnetic Materials* **2018,** *462*, 185-194.

6. Podaru, G. V.; Chikan, V.; Prakash, P., Magnetic Field Induced Ultrasound from Colloidal Superparamagnetic Nanoparticles. *The Journal of Physical Chemistry C* **2016,** *120* (4), 2386-2391.

7. Podaru, G.; Ogden, S.; Baxter, A.; Shrestha, T.; Ren, S.; Thapa, P.; Dani, R. K.; Wang, H.; Basel, M. T.; Prakash, P.; Bossmann, S. H.; Chikan, V., Pulsed magnetic field induced fast drug release from magneto liposomes via ultrasound generation. *The Journal of Physical Chemistry. B* **2014,** *118* (40), 11715-22.

8. Carrey, J.; Connord, V.; Respaud, M., Ultrasound generation and high-frequency motion of magnetic nanoparticles in an alternating magnetic field: Toward intracellular ultrasound therapy? *Applied Physics Letters* **2013,** *102* (23), 232404.

9. Kumar, C. S.; Mohammad, F., Magnetic nanomaterials for hyperthermia-based therapy and controlled drug delivery. *Advanced Drug Delivery Reviews* **2011,** *63* (9), 789-808.

10. Bi, H.; Han, X., Magnetic field triggered drug release from lipid microcapsule containing lipid-coated magnetic nanoparticles. *Chemical Physics Letters* **2018,** *706*, 455-460.

11. Nardoni, M.; Della Valle, E.; Liberti, M.; Relucenti, M.; Casadei, M. A.; Paolicelli, P.; Apollonio, F.; Petralito, S., Can Pulsed Electromagnetic Fields Trigger On-Demand Drug Release from High-Tm Magnetoliposomes? *Nanomaterials (Basel)* **2018,** *8* (4).

12. Q. A. Pankhurst, J. C., S. K. Jones, J. Dobson, Applications of magnetic nanoparticles in biomedicine. *Jurnal of Physics D: Applied Physics* **2003,** *36*, 167-181.

13. Zarschler, K.; Rocks, L.; Licciardello, N.; Boselli, L.; Polo, E.; Garcia, K. P.; De Cola, L.; Stephan, H.; Dawson, K. A., Ultrasmall inorganic nanoparticles: State-of-the-art and perspectives for biomedical applications. *Nanomedicine : Nanotechnology, Biology and Medicine* **2016,** *12* (6), 1663-701.

14. Lakshmanan, S.; Gupta, G. K.; Avci, P.; Chandran, R.; Sadasivam, M.; Jorge, A. E.; Hamblin, M. R., Physical energy for drug delivery; poration, concentration and activation. *Advanced Drug Delivery Reviews* **2014,** *71*, 98-114.

15. Du, X.; Wang, J.; Zhou, Q.; Zhang, L.; Wang, S.; Zhang, Z.; Yao, C., Advanced physical techniques for gene delivery based on membrane perforation. *Drug Delivery* **2018,** *25* (1), 1516-1525.

16. Kardos, T. J.; Rabussay, D. P., Contactless magneto-permeabilization for intracellular plasmid DNA delivery in-vivo. *Human Vaccines & Immunotherapeutics* **2012,** *8* (11), 1707-13.

17. Novickij, V.; Grainys, A.; Novickij, J.; Markovskaja, S., Irreversible magnetoporation of micro-organisms in high pulsed magnetic fields. *IET Nanobiotechnology* **2014,** *8* (3), 157-62.

18. Rosensweig, R. E., Heating magnetic fluid with alternating magnetic field. *Journal of Magnetism and Magnetic Materials* **2002,** *252*, 370-374.

19. Usadel, K. D., Dynamics of magnetic nanoparticles in a viscous fluid driven by rotating magnetic fields. *Physical Review B* **2017,** *95* (10).

20. Babincova, N.; Sourivong, P.; Babinec, P.; Bergemann, C.; Babincova, M.; Durdik, S., Applications of magnetoliposomes with encapsulated doxorubicin for integrated chemotherapy and hyperthermia of rat C6 glioma. *Zeitschrift fur Naturforschung. C, Journal of Biosciences* **2018,** *73* (7-8), 265-271.

21. Shirmardi Shaghasemi, B.; Virk, M. M.; Reimhult, E., Optimization of Magneto-thermally Controlled Release Kinetics by Tuning of Magnetoliposome Composition and Structure. *Scientific Reports* **2017,** *7* (1), 7474.

22. Zubaidah, T.; Kanata, B.; Paniran, Three-dimensional Mapping of Static Magnetic Fields over a Semi-anechoic Chamber. *International Journal of Technology* **2014,** *5*, 209-218.

23. Extavour, M., Design and construction of magnetic elements for trapping and transport of cold neutral atoms. **2004**.

24. Skumiel, A.; Leszczyński, B.; Molcan, M.; Timko, M., The comparison of magnetic circuits used in magnetic hyperthermia. *Journal of Magnetism and Magnetic Materials* **2016,** *420*, 177-184.

25. Podaru, G.; Moore, J.; Dani, R. K.; Prakash, P.; Chikan, V., Nested Helmholtz coil design for producing homogeneous transient rotating magnetic fields. *The Review of Scientific Instruments* **2015,** *86* (3), 034701.

26. LibreTexts Physics 11.2: Magnetic Fields and Lines. https://phys.libretexts.org/Bookshelves/University_Physics/Book%3A_University_Physics_(OpenStax)/Map%3A_University_Physics_II_-_Thermodynamics%2C_Electricity%2C_and_Magnetism_(OpenStax)/11%3A_Magnetic_Forces_and_Fields/11.2%3A_Magnetic_Fields_and_Lines (last updated October 13, 2019; accessed November 13, 2019).

27. Tumanski, S., Induction coil sensors—a review. *Measurement Science and Technology* **2007,** *18* (3), R31-R46.

28. Lemal, P.; Geers, C.; Rothen-Rutishauser, B.; Lattuada, M.; Petri-Fink, A., Measuring the heating power of magnetic nanoparticles: an overview of currently used methods. *Materials Today: Proceedings* **2017,** *4*, S107-S117.

29. Wildeboer, R. R.; Southern, P.; Pankhurst, Q. A., On the reliable measurement of specific absorption rates and intrinsic loss parameters in magnetic hyperthermia materials. *Journal of Physics D: Applied Physics* **2014,** *47* (49), 495003.

# Appendix A - Computer codes

## Appendix 1 Matlab function used to calculate the resonance frequency of the coils

```
function [] = pulsewaveform()
%PULSEWAVEFORM Applying Fourier transformation to time domain
data of the electromagnetic pulses.

%% Loading data from file

data1=load('C1a-H pulse00000.txt','-ascii');
data2=load('C1a-H pulse00001.txt','-ascii');
data3=load('C1a-H pulse00002.txt','-ascii');
data4=load('C1a-H pulse00003.txt','-ascii');
data5=load('C1H pulse00000.txt','-ascii');
data6=load('C1H pulse00001.txt','-ascii');
data7=load('C1H pulse00002.txt','-ascii');
data8=load('C1H pulse00003.txt','-ascii');
data9=load('C1H pulse00004.txt','-ascii');

%% Processing raw data

% Combining time and amplitude data into two arrays
t=[data1(:,1) data2(:,1) data3(:,1) data4(:,1) data5(:,1)
data6(:,1)...
    data7(:,1) data8(:,1) data9(:,1)];
I=[data1(:,2) data2(:,2) data3(:,2) data4(:,2) data5(:,2)
data6(:,2)...
    data7(:,2) data8(:,2) data9(:,2)];

% Calculating the average amplitude of nine measurements to
decrease noise.
tavg=mean(t,2);
Iavg=mean(I,2);

tdata=[tavg Iavg]; % creating a single array of the data for
saving
csvwrite('Cart coil pulse waveform.csv', tdata); % Saving the
data

%% Plotting the averaged waveform
figure() % Creating new figure window
plot(tavg,Iavg); % Reating a lineplot of the averaged waveform
xlim([-1e-4 3e-4]); % Seting the limts of the X axis
```

```
ylim([-1.5 1.5]); % Seting the limts of the Y axis
xlabel('Time (s)'); % Creating axis label for the X axis
ylabel('Amplitude (V)'); % Creating axis label for the Y axis
set(gcf,'color','w'); % Setting background color to white for
publication

%% Applying Fourier-transformation

Y=fft(Iavg); % Taking the Fourier-transform of the averaged
amplitude data
f = ((0:length(Y)-1)*250000000/length(Y))'; % Creating a
frequency-scale...
% based on the sampling frequency (250 MS/s) and number of
datapoints

fdata=[f Y]; % Creating a single array of the data for saving
csvwrite('Cart coil pulse frequency.csv', fdata); % Saving the
data

[value index]=max(Y); % Finding the amplitude maximum in the
data.
fmax=f(index); % Finding the peak position of the maximum.

%% Plotting the Fourier-transformed data
figure() % Creating a new figure window
semilogx(f,abs(Y),fmax,abs(Y(index)),'O'); % Creating a
semilogarithmic
% plot of the Fourier-transformed data

set(gcf,'color','w'); % Setting background color to white for
publication
xlabel('Frequency (Hz)'); % Creating axis label for the X axis
ylabel('Amplitude'); % Creating axis label for the Y axis
annotation('textbox', [0.4, 0.75, 0.1, 0.1], 'String',...
    "Resonance frequency: " + fmax + ' Hz') % Displaying
resonance freq.
xlim([900 1e8]) % Seting the limts of the X axis
ylim([0 5000]) % Seting the limts of the Y axis

end
```

# Appendix 2 Magnetic pulse instrument main control program

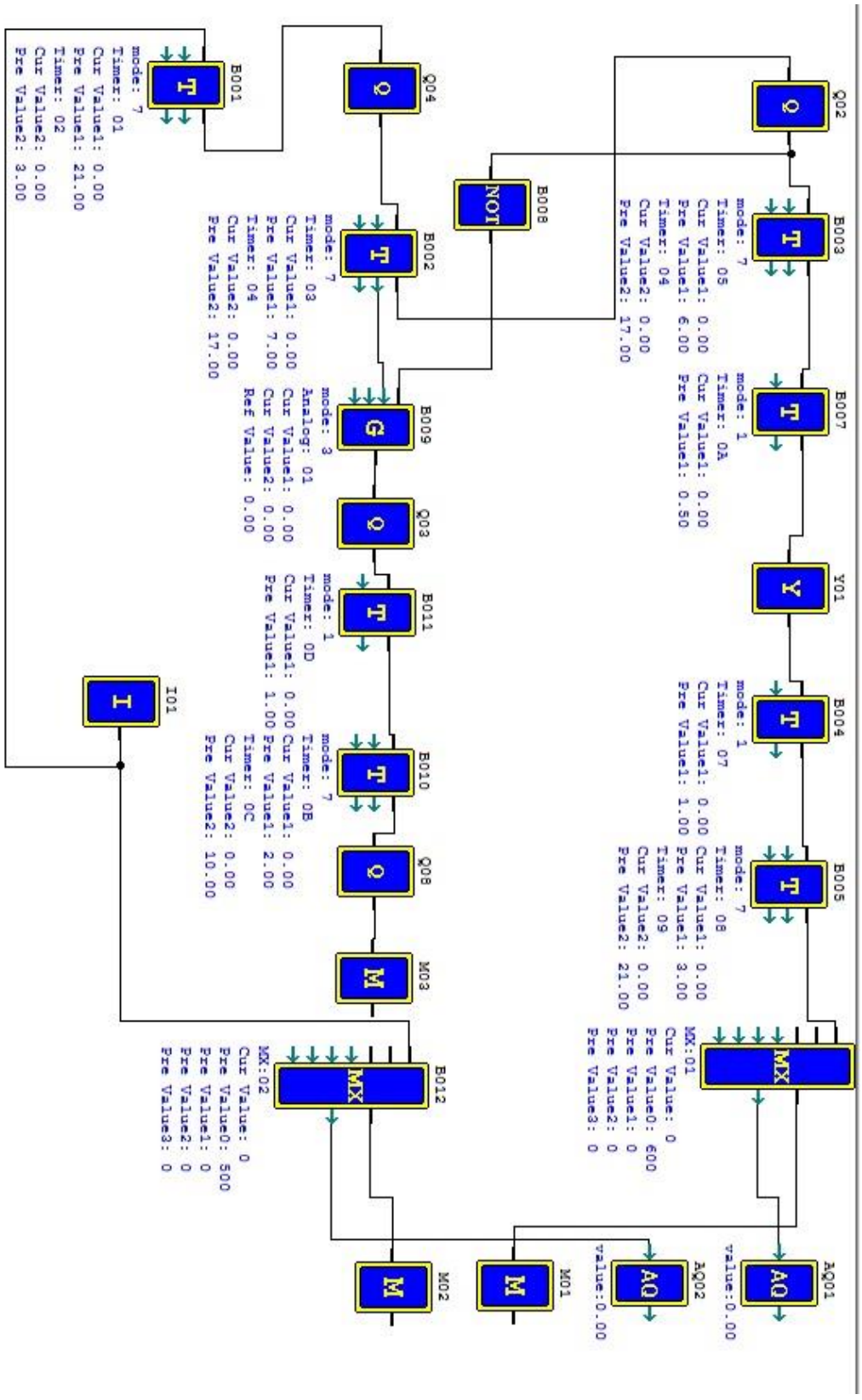

## Appendix 3 Arduino trigger signal program

```
int sensorPin = A0;    // select the input pin for the potentiometer-analog input
int ledPin = 13;      // select the pin for the digital output Note you can use it to test pin13
is the LED!
float sensorValue = 0;  // variable to store the value coming from the sensor
float voltage;

void setup() {
  // declare the ledPin as an OUTPUT:
  pinMode(ledPin, OUTPUT);
  Serial.begin(9600);
}

void loop() {
  // read the value from the sensor:
  sensorValue = analogRead(sensorPin);
voltage= sensorValue * (5.0 / 1023.0);
Serial.println(voltage);
  delay(1);
  if (voltage > 4){
    for (int i=0; i <= 4; i++){
    digitalWrite(13, HIGH);
    delay(20);
    digitalWrite(13, LOW);
    delay(20);
    }

}

}
```

## Appendix 4 Matlab function used to fit the experimental data and calculate the initial slope of the heating curve

```
function [] = initial_slope()

%%%%%%%%%%%%%%%%%%%%%%%%%%%%%%%%%%%%%%%%%%%%%%%%%%%%%%%%%%%%%%%%%%%%%%%%
% Loading data,extracting measurement parameters from filename %
%%%%%%%%%%%%%%%%%%%%%%%%%%%%%%%%%%%%%%%%%%%%%%%%%%%%%%%%%%%%%%%%%%%%%%%%
filename='…….txt'; %selecting file to open
[filepath,name,ext]=fileparts(filename); % extracting filename
inner=convertCharsToStrings(strrep(name(10:12),',','.')); %
extracting inner coil voltage
outer=convertCharsToStrings(strrep(name(15:17),',','.')); %
extracting outer coil voltage

data=load(filename, '-ascii'); % loading data
x=data(:,1); % creating array of x elements (time vector)
y=data(:,2); % creating array of y elements (temperature data)

%%%%%%%%%%%%%%%%%%%%%%%%%%%%%%%%%%%%%%%%%%%%%%%%%%%%%%%%%%%%%%%%%%%%%%%%
% Baseline correction and timescale adjustment %
%%%%%%%%%%%%%%%%%%%%%%%%%%%%%%%%%%%%%%%%%%%%%%%%%%%%%%%%%%%%%%%%%%%%%%%%
ycorr=y-y(1); % calculating temperature change
xslim=x(301:751); % selecting x data of the first 7.5 minutes
ycorrslim=ycorr(301:751); % selecting y data of the first 7.5
minutes, discarding the first few seconds
xcorrslim=xslim/60-(xslim(1)/60); % converting time unit to
minutes

%%%%%%%%%%%%%%%%%%%%%%%%%%%%%%%%%%%%%%%%%%%%%%%%%%%%%%%%%%%%%%%%%%%%%%%%
% Fitting experimental data and evaluating fit %
%%%%%%%%%%%%%%%%%%%%%%%%%%%%%%%%%%%%%%%%%%%%%%%%%%%%%%%%%%%%%%%%%%%%%%%%
[p]=polyfit(xcorrslim,ycorrslim,2); % getting coefficients of
the fitted polynomial
xfit=linspace(0,4.5,100)'; % creating time vector for the fitted
polynomial
yfit=polyval(p,xfit); % calculating fitted curve for the
selected time vector

%%%%%%%%%%%%%%%%%%%%%%%%%%%%%%%%%%%%%%%%%%%%%%%%%%%%%%%%%%%%%%%%%%%%%%%%
% Differentiating curve, determining initial slope %
%%%%%%%%%%%%%%%%%%%%%%%%%%%%%%%%%%%%%%%%%%%%%%%%%%%%%%%%%%%%%%%%%%%%%%%%
diffp=polyder(p); % differentiating the polynomial
```

```
slopes=polyval(diffp,xfit); % evaluating dy/dx for the created
time vector
m0=diffp(1,2); % initial slope is the intercept of the dy/dx
line
b=p(1,3); % intercept of the tangent line at x=1 point is the
intercept of the original polynomial
inslopeline=m0*xfit+b; % calculating y values for the initial
slope tangent line

%%%%%%%%%%%%%%%%%%%%%%%%%%%%%%%%%%%%%%%%%%%%%%%
% Plotting experimental and fitted data %
%%%%%%%%%%%%%%%%%%%%%%%%%%%%%%%%%%%%%%%%%%%%%%%
%subplot(1,2,1); % creating 1st subplot
hold on % plot commands between hold on and off will not
overwrite previous lines on the figure
plot(xfit,yfit,'r','LineWidth',1.5); % plotting fitted line
plot(xcorrslim,ycorrslim,'k','LineWidth',0.5); % plotting
experimental data
plot(xfit,inslopeline,'b--'); % plotting initial slope tangent
line
xlabel('Time (min)');
ylabel('Temperature change (Celsius)');
legend('Fitted line','Measured data','Initial slope');
%xlim([0 4.6]);
%ylim([0,1.6]);
formatSpec2='m_{04=%.5f deg/min';
str=sprintf(formatSpec2,m0);
%text(2,0,str);
hold off

%subplot(1,2,2); % creating 2nd subplot
%plot(xfit,slopes);
%xlabel('Time (min)');
%ylabel('Slope (Degrees/min)');

formatSpec = 'The initial slope is %d degrees per minute.';
sprintf(formatSpec, m0) % printing out initial slope value

%%%%%%%%%%%%%%%%%%%%%%%%%%%%%%%%%%%%%%%%%%%%%%%%%%%%%%%%%%%%
% Saving parameters and slope values to .txt file %
%%%%%%%%%%%%%%%%%%%%%%%%%%%%%%%%%%%%%%%%%%%%%%%%%%%%%%%%%%%%
formatSpec3='%s\t%s\t%s';
m0tosave=sprintf(formatSpec3,inner,outer,num2str(m0,4));
dlmwrite('E:\Documents\PhD\Research\Magnetic heating\initial
slopes for concentrated NP solution.txt',m0tosave,'-
append','delimiter','','newline','pc')
end
```